

Western Kentucky University
TopSCHOLAR®

Masters Theses & Specialist Projects

Graduate School

8-2013

Synthesis and Computational Studies of a New
Class of Lanthanide Niobate Cluster :
 $[\text{Ln}_4(\text{H}_2\text{O})_8(\text{SO}_4)_5(\text{NbO}_3)_2]+3\text{H}_2\text{O}$; Ln= Dy,
Tb

Brady D. Garabato

Western Kentucky University, brady.garabato874@topper.wku.edu

Follow this and additional works at: <http://digitalcommons.wku.edu/theses>

 Part of the [Environmental Chemistry Commons](#), [Inorganic Chemistry Commons](#), and the [Physical Chemistry Commons](#)

Recommended Citation

Garabato, Brady D., "Synthesis and Computational Studies of a New Class of Lanthanide Niobate Cluster : $[\text{Ln}_4(\text{H}_2\text{O})_8(\text{SO}_4)_5(\text{NbO}_3)_2]+3\text{H}_2\text{O}$; Ln= Dy, Tb" (2013). *Masters Theses & Specialist Projects*. Paper 1294.
<http://digitalcommons.wku.edu/theses/1294>

This Thesis is brought to you for free and open access by TopSCHOLAR®. It has been accepted for inclusion in Masters Theses & Specialist Projects by an authorized administrator of TopSCHOLAR®. For more information, please contact topscholar@wku.edu.

SYNTHESIS AND COMPUTATIONAL STUDIES OF A NEW CLASS OF
LANTHANIDE NIOBATE CLUSTER: $[\text{Ln}_4(\text{H}_2\text{O})_8(\text{SO}_4)_5(\text{NbO}_3)_2] \cdot 3\text{H}_2\text{O}$; Ln= Dy, Tb

A Thesis
Presented to
The Faculty of the Department of Chemistry
Western Kentucky University
Bowling Green, Kentucky

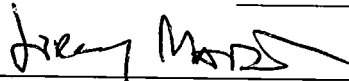
In Partial Fulfillment
of the Requirement for the Degree
Master of Science

By
Brady D. Garabato

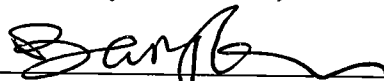
August 2013

SYNTHESIS AND COMPUTATIONAL STUDIES OF A NEW CLASS OF
LANTHANIDE NIOBATE CLUSTER: $[\text{Ln}_4(\text{H}_2\text{O})_8(\text{SO}_4)_5(\text{NbO}_3)_2] \cdot 3\text{H}_2\text{O}$; Ln= Dy, Tb

Date Recommended July 9, 2013




Dr. Jeremy B. Maddox, Co-director of Thesis



Dr. Bangbo Yan, Co-director of Thesis



Dr. Eric Conte


Dean, Graduate Studies and Research

8-19-13
Date

ACKNOWLEDGMENTS

I would like to sincerely thank my advisors Dr. Jeremy B. Maddox and Dr. Bangbo Yan for their patience, guidance, and support. They have strengthened my foundation as researcher, and as a person, and I will always be grateful for their examples. I would also like to acknowledge the following institutions at Western Kentucky University: the Bioinformatics and Information Science Center for funding my computational studies, the High Performance Computing Center for their computational resources, the Advanced Materials Institute for the TGA, Dr. Aaron Celestian for his expertise with the powder XRD, and the Department of Graduate Studies.

TABLE OF CONTENTS

ABSTRACT	viii
CHAPTER I INTRODUCTION.....	1
Outline.....	1
Introduction.....	1
CHAPTER II LITERATURE REVIEW	4
Outline.....	4
Introduction.....	4
Hybrid Lanthanide Polyoxomolybdates (POMo)	6
Hybrid Lanthanide Polyoxovanadates (POV)	7
Hybrid Lanthanide Polyoxoniobates (PONb).....	9
Computational Methods for Polyoxometalates.....	11
CHAPTER III TWO ISOSTRUCTURAL LANTHANIDE POLYOXONIOBATES.....	13
Outline.....	13
Synthesis of $[\text{Dy}_4(\text{H}_2\text{O})_8(\text{SO}_4)_5(\text{NbO}_3)_2] \cdot 3\text{H}_2\text{O}$	13
Synthesis of $[\text{Tb}_4(\text{H}_2\text{O})_8(\text{SO}_4)_5(\text{NbO}_3)_2] \cdot 3\text{H}_2\text{O}$	14
Structures of $[\text{Dy}_4(\text{H}_2\text{O})_8(\text{SO}_4)_5(\text{NbO}_3)_2] \cdot 3\text{H}_2\text{O}$ and $[\text{Tb}_4(\text{H}_2\text{O})_8(\text{SO}_4)_5(\text{NbO}_3)_2] \cdot 3\text{H}_2\text{O}$	14
Powder X-Ray Diffraction (PXRD) of $[\text{Ln}_4(\text{H}_2\text{O})_8(\text{SO}_4)_5(\text{NbO}_3)_2] \cdot 3\text{H}_2\text{O}$; Ln= Dy, Tb	19
Thermal Gravimetric Analysis (TGA) of $[\text{Ln}_4(\text{H}_2\text{O})_8(\text{SO}_4)_5(\text{NbO}_3)_2] \cdot 3\text{H}_2\text{O}$; Ln= Dy, Tb	21

Solid UV-Vis Spectra of [Ln ₄ (H ₂ O) ₈ (SO ₄) ₅ (NbO ₃) ₂]·3H ₂ O; Ln= Dy, Tb	22
Solid Luminescence-Emission Spectra of [Ln ₄ (H ₂ O) ₈ (SO ₄) ₅ (NbO ₃) ₂]·3H ₂ O; Ln= Dy, Tb	23
CHAPTER IV COMPUTATIONAL METHODS	25
Outline.....	25
Electronic Structure Calculations and Optical Spectra.....	25
Dy ₄ Nb ₂ (SO ₄) ₅	25
Dy ₄ Nb ₂ (SO ₄) ₄ TD-DFT Geometries	26
CHAPTER V CONCLUSIONS	35
Outline.....	35
Summary	35
APPENDIX A Computational Terms.....	37
Density Functional Theory	37
Geometry Optimizations and Normal Modes Frequency Analysis.....	38
Time Dependent Density Functional Theory.....	38
Natural Transition Orbital Analysis.....	39
APPENDIX B Development of Computational methods.....	41
Calcium Metal Organic Frameworks.....	41
Free acids (H ₃ btc and Hpzc) and ions (btc and pzc) in water.....	42
H ₃ btc in Water.....	42
Hpzc in Water	46
btc and pzc ions in water.....	48
Compound 1	51

Coordination Environments	53
Benchmark Calculations with Pseudopotential Basis Sets	54
REFERENCES	59

LIST OF FIGURES

Figure 1. $[\text{Cr}_2(\text{OH})_4\text{Nb}_{10}\text{O}_{30}]^{8-}$	11
Figure 2. Structure of $\text{Ln}_4(\text{H}_2\text{O})_8(\text{SO}_4)_5(\text{NbO}_3)_2 \cdot 3\text{H}_2\text{O}$, Ln=Tb, Dy	14
Figure 3. Structure of $[\text{Dy}_4(\text{H}_2\text{O})_8(\text{SO}_4)_5(\text{NbO}_3)_2] \cdot 3\text{H}_2\text{O}$	15
Figure 4. Structure of $[\text{Tb}_4(\text{H}_2\text{O})_8(\text{SO}_4)_5(\text{NbO}_3)_2] \cdot 3\text{H}_2\text{O}$	17
Figure 5. Simulated and experimental PXRD of $[\text{Dy}_4(\text{H}_2\text{O})_8(\text{SO}_4)_5(\text{NbO}_3)_2] \cdot 3\text{H}_2\text{O}$	19
Figure 6. Simulated and experimental PXRD of $[\text{Dy}_4(\text{H}_2\text{O})_8(\text{SO}_4)_5(\text{NbO}_3)_2] \cdot 3\text{H}_2\text{O}$	20
Figure 7. TGA of $[\text{Dy}_4(\text{H}_2\text{O})_8(\text{SO}_4)_5(\text{NbO}_3)_2] \cdot 3\text{H}_2\text{O}$ and $[\text{Tb}_4(\text{H}_2\text{O})_8(\text{SO}_4)_5(\text{NbO}_3)_2] \cdot 3\text{H}_2\text{O}$	21
Figure 8. Solid UV-Vis spectra of $[\text{Dy}_4(\text{H}_2\text{O})_8(\text{SO}_4)_5(\text{NbO}_3)_2] \cdot 3\text{H}_2\text{O}$ and $[\text{Tb}_4(\text{H}_2\text{O})_8(\text{SO}_4)_5(\text{NbO}_3)_2] \cdot 3\text{H}_2\text{O}$	22
Figure 9. Solid Luminescence-emission spectra of $[\text{Dy}_4(\text{H}_2\text{O})_8(\text{SO}_4)_5(\text{NbO}_3)_2] \cdot 3\text{H}_2\text{O}$ and $[\text{Tb}_4(\text{H}_2\text{O})_8(\text{SO}_4)_5(\text{NbO}_3)_2] \cdot 3\text{H}_2\text{O}$	23
Figure 10. $\text{Dy}_4\text{Nb}_2(\text{SO}_4)_5$ optimized geometry from SXRD structure	25
Figure 11. $\text{Dy}_4\text{Nb}_2(\text{SO}_4)_4$ TD-DFT geometries	26
Figure 12. Calculated and experimental spectra of A^{2+} and A^0	27
Figure 13. NTO hole/particle pairs for A^{2+}	28
Figure 14. NTO hole/particle pairs for A^0	29
Figure 15. Calculated and experimental spectra of B^0 with M06Land BP86	30
Figure 16. NTO hole/particle pairs for B^0 M06L	31
Figure 17. NTO hole/particle pairs for B^0 BP86	32
Figure 18. TD-DFT of geometry A^0 with different functionals	34
Figure 19. Coordination environments in compound 1	41

Figure 20. Calculated and experimental UV spectra of H ₃ btc in water.....	43
Figure 21. NTO hole/particle pairs for H ₃ btc at 253 nm.....	44
Figure 22. NTO hole/particle pairs for H ₃ btc at 242 nm.....	45
Figure 23. NTO hole/particle pairs for H ₃ btc at 229 nm.....	45
Figure 24. NTO hole/particle pairs for H ₃ btc at 217 nm.....	46
Figure 25. Calculated and experimental UV spectra of Hpzc in water	47
Figure 26. NTO hole/particle pairs for Hpzc at 254 and 219 nm	48
Figure 27. Calculated UV spectrum of btc and pzc ions in water	49
Figure 28. NTO hole/particle pairs for btc ion at 323 nm	50
Figure 29. NTO hole/particle pairs for btc ion at 221 nm	51
Figure 30. NTO hole/particle pairs for btc ion at 208 nm	51
Figure 31. Calculated UV spectra for btc and pzc from SXRD data.....	52
Figure 32. Rydberg particle state of Calcium coordination environment.....	54
Figure 33. Calculated and experimental UV spectra of Eu ^{III} acetate.....	56
Figure 34. Calculated and experimental UV spectra of Eu ^{III} nitrate.....	57
Figure 35. TD-DFT spectra of theoretical Eu-Nb ₆ O ₁₉	57

LIST OF TABLES

Table 1. Crystallographic data for $[\text{Dy}_4(\text{H}_2\text{O})_8(\text{SO}_4)_5(\text{NbO}_3)_2] \cdot 3\text{H}_2\text{O}$	16
Table 2. Crystallographic data for $[\text{Tb}_4(\text{H}_2\text{O})_8(\text{SO}_4)_5(\text{NbO}_3)_2] \cdot 3\text{H}_2\text{O}$	18

SYNTHESIS AND COMPUTATIONAL STUDIES OF A NEW CLASS OF
LANTHANIDE NIOBATE CLUSTER: $[\text{Ln}_4(\text{H}_2\text{O})_8(\text{SO}_4)_5(\text{NbO}_3)_2] \cdot 3\text{H}_2\text{O}$; Ln= Dy, Tb

Brady Garabato

August 2013

66 Pages

Directed By: Dr. Jeremy B. Maddox, Dr. Bangbo Yan, and Dr. Eric Conte

Department of Chemistry

Western Kentucky University

Polyoxoniobates (PONbs) are a small family of highly electron-rich clusters. The development of new solids composed of these clusters have applications in green energy and electronics. However, the high charge environment of PONbs typically requires alkaline synthetic conditions that are unsuitable for introducing other metals and organic molecules, making synthesis of new systems difficult. To date, very few transition metals and organic ligands have been incorporated into these PONb solids, and lanthanide metal inclusion, which generally improves photoconductivity due to long-lived *f*-orbital excitations, has not yet been fully realized. Here, the synthesis of a new class of lanthanide niobate cluster $[\text{Ln}_4(\text{H}_2\text{O})_8(\text{SO}_4)_5(\text{NbO}_3)_2] \cdot 3\text{H}_2\text{O}$; Ln= Dy, Tb under acidic conditions is reported.

Structures were determined by crystallography and time-dependent density functional theory (TD-DFT) was used to provide insight into photo-induced electronic transitions. Supporting computational methods that are currently being developed for modeling these emerging cluster systems are described.

CHAPTER I INTRODUCTION

Outline

This chapter discusses the relevance of new solid-state materials for optimizing current green energy applications. The structure and properties of these emerging solids are introduced and the major directions of research in this field are identified.

Introduction

Understanding electron transfer in emergent photoactive systems is a fundamental challenge in the development of optimized materials for green energy applications. Although the production of an electric current from light is generally well understood, this understanding is based upon the most widely used photoconductive technology— the silicon photovoltaic (PV) cell. In order to improve the efficiency of PV materials, as well as develop novel ways that photocurrent can be utilized, a broader perspective of photoconductivity is necessary. Systems that utilize light for other applications besides generating an electric current include photocatalysts that convert CO₂ into green fuels like methanol or ethanol, or porous materials that store hydrogen, or other molecules for photochemical reactions.¹ The United States Department of Energy (DOE) projects CO₂ emissions from fossil fuels to decline due to new emission standards, and increased funding for new non-petroleum energy sources.² In the same annual report, the DOE expects that nuclear power will account for much more of the nation's electricity generation in the future by providing nuclear energy incentives, funding for building new plants, and research into small scale reactors. Moving away from fossil fuels will also require the development of improved materials for green energy applications.

Silicon solar cells, which are currently the most energy efficient solar technology, have power efficiencies around 18%, with theoretical limits around 32%.³ Hydrogen production from water hydrolysis using current electrolyzers is very efficient, at around 80%— making maximum photovoltaic-driven hydrolysis around 14% efficient, with a theoretical limit of 24%. Although these theoretical limits seem discouraging at first, they could be raised up to 40% by developing tandem systems, such as those optimized for water oxidation and hydrogen production.³ Furthermore, photosystems that could generate multiple charge carriers per absorbed photon, absorb UV light more efficiently, or absorb IR photons, and could raise the theoretical thermodynamic limit to 66%.³

Regardless of the application, the components of any photoactive system have one thing in common— the need for a better way to conduct electricity produced by light. In general this means two things: absorbing light more efficiently, and making the charge produced last much longer. One of the biggest trade-offs here is that with current materials, lowering the energy it takes to absorb a photon or shift the system to absorb more visible light, makes the lifetime of the charge produced much shorter. Increasing the charge lifetime of a system could be done by raising its absorption energy, i.e., shifting its absorbance to the UV region. However, while UV photoconductivity is very efficient itself, the majority of sunlight is not ultraviolet, which makes overall efficiencies in current solar devices low. Indeed, much of the current research in photovoltaics is directed at increasing the range of available light that may be used to produce electricity.

Rare-earth, or lanthanide metals have been shown to improve photovoltaic devices in simple sandwich-type active layers. This is likely due to the long lifetime of excited states in rare-earth metals, which decay through phosphorescence.⁴ Organic

molecules such as dyes are also commonly used to extend the range of light into the visible region. Solid-state materials, which contain organic dyes, lanthanide-transition metal clusters, and polyoxometalate (POM) clusters are developing technologies. POM systems show promise in optimizing the photoconductivity of lanthanide hybrid systems because of their high charge density, which provides the photosystem with many electrons per atom.⁴ While some POM-lanthanide systems that include organic ligands have been realized in the last decade, this field is relatively underdeveloped, and inclusion of higher charge density POMs, like PONbs, into these systems remains largely incomplete. Although not entirely understood, the charge transfer properties of emerging lanthanide and POM systems present new possibilities for known systems, and are also desirable synthetic targets towards more efficient green energy applications.

CHAPTER II LITERATURE REVIEW

Outline

This chapter introduces the structure and properties of metal-organic framework (MOF), and polyoxometalate (POM) solids. This chapter reviews lanthanide metal inclusion in organic-POM solids, and includes the POMs composed of the metals W, V, Mo, and Nb. The purpose of this review is to identify undeveloped lanthanide POM materials, and validate the synthetic pursuit of an optimized target system composed of Nb. This chapter also reviews the few current computational methods used for POM excited states, validating the need to develop TD-DFT methods for emerging lanthanide-POMs to provide insight into their electronic structure, and electron-transfer.

Introduction

The advancement of green energy applications will be accelerated through the optimization of atomically engineered photoactive materials.¹ Solar cells, hydrogen fuel cells, and reduction of carbon dioxide to green fuels, such as ethanol and methanol, are examples of applications that would benefit from the development of new inorganic materials. Metal-organic frameworks (MOFs) and polyoxometalates (POMs) are two of the major classifications of materials that have attracted extensive research studies because of their potential applications in these areas.

The term hybrid is used to describe a system that contains both organic molecules and inorganic metals—the connecting bridges that create extended structures such as MOFs. The oxygen or nitrogen groups contained within ligands, are considered the ends of a bridge, and bonds to transition metals or other atoms act as anchoring points for the linkages. Some ligands, such as 2,2-bipyridine “cap” a metal, by forming multiple

coordinate covalent bonds to the metal and leaving other sites on the metal for linking. Aromatic ligands are generally better at absorbing light than the smaller organic ligands, and as such are desirable to use as linkers in photovoltaic applications. Transition metals have been the most common metallic species used in MOF chemistry; however, in recent years both main group and rare earth metals have also been incorporated into metal-organic network topologies.⁸

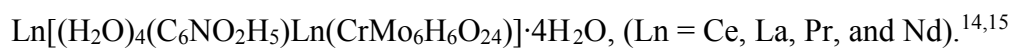
Polyoxometalates (POMs), i.e., metal-oxide anionic clusters of various sizes, have also been linked together by organic ligands to form MOFs.⁹ POM clusters are generally composed of tungsten, molybdenum, vanadium, or niobium. Ligands may also be used to connect other metals to POM clusters, and even link these clusters together. The photoactivity of POMs is of great interest in modern inorganic chemistry due to their high charge densities, and versatile coordination environments. In POMs, transition metals typically have high oxidation states, and when co-coordinated to several oxygens, provide a rich electron source in photoactive systems. Furthermore, certain aromatic ligands have the desirable property of absorbing visible light, whereas POMs by themselves typically absorb in the UV range. This is significant in developing green applications because new charge-dense, porous materials that absorb more of the visible spectrum of light are possible.

Rare earth metals, or lanthanides, exhibit novel electronic and optical properties due to their partially filled f atomic orbitals. One such property is phosphorescence; the spin-forbidden radiative relaxation of a photoexcited electron to the ground state from an f orbital. The long relaxation rates of rare earth phosphorescence increases charge-lifetime in hybrid systems, making rare earth metals ideal candidates as co-sensitizers towards the

photoconductive optimization of hybrid POM systems.⁴ There are relatively few rare-earth MOFs reported, and even fewer examples incorporating POMs. Although lanthanide coordination polymers have been extensively studied, the inclusion of POMs into the diverse chemistry of lanthanide polymeric networks remains incomplete.¹⁰ The lanthanide POMs that are known are mainly in the tungsten POM family. However, tungsten POMs have also been extensively researched. Non-tungsten POMs— those containing molybdenum, vanadium, and niobium, have higher charge densities per atom and thus the potential, with additional research, to produce more photocurrent and become viable candidates for green energy applications. The focus of this review is primarily on the importance of developing molybdenum (POMo), vanadium (POV), and niobium (PONb) for photovoltaic applications.

Hybrid Lanthanide Polyoxomolybdates (POMo)

Of the POMs considered in this review, it is easiest to attach rare earth metals and organic ligands to those containing molybdenum (POMo). This makes POMo ideal candidates, for the development of new hybrid rare-earth POMs. The potential systems that may be developed from current lanthanide-POMo and hybrid POMo systems are promising. Aromatic nitrogen containing ligands, such as imidazole and bi-imidazole, coordinated to metals, such as Co, Zn, Na and Ni, have been shown to coordinate with POMo, although without lanthanides, in hydrothermal work-ups.¹¹⁻¹³ An, et. al, have recently developed the only known POMo series that contains both rare-earth atoms and organic molecules. Their structures are a family of α -chromium polyoxomolybdates coordinated to aromatic amines of the form



Other groups have developed POMo with cores consisting of multiple lanthanide atoms.¹⁶⁻¹⁸ These cores vary in size from two to several lanthanides, and are decorated by POMo clusters of different sizes. However, these POMo do not contain organic molecules. Adopting synthetic procedures similar to those of An et. al, and precursor POMo containing complex rare earth cores, such as those of Yamase, new POM structures with organic ligands suitable for green energy applications may be possible.¹⁶

Hybrid Lanthanide Polyoxovanadates (POV)

In contrast to POMo, there are only two polyoxovanadates (POV) that contain a lanthanide metal, and none that contain both lanthanides and organic ligands. The two known lanthanide POV have the formulas $[\text{Ln}(\text{H}_2\text{O})_7]_2[\text{V}_{10}\text{O}_{28}] \cdot 11\text{H}_2\text{O}$; (Ln= Ce, Gd), and $[\{\text{Ln}(\text{H}_2\text{O})_7\}_2\text{As}_6\text{V}_{15}\text{O}_{42}(\text{H}_2\text{O})] \cdot n\text{H}_2\text{O}$ (Ln= La, Sm, Ce).^{19, 9} However, the POV clusters are likely the easiest of the POMs to complex with transition metals and organic ligands. Hybrid POV chemistry is rich with new systems that have been developed, and has recently been reviewed elsewhere.²⁰ The diversity in POV chemistry is due to a range of stable synthetic intermediates. These intermediates proceed through the oxidation of reduced metavanadate, or through the coordination of a metavanadate species directly to a transition metal cation. These stable intermediates, composed of metavanadates and transition metals, are accessible even in highly acidic environments, giving rise to a chemistry that is easily adaptable to other systems.²⁰ Hybrid POV are mainly composed of small clusters, the Lindqvist type cluster containing six vanadium atoms, or the lacunary kegglin structure, a type of “sandwich” composed of other small cluster fragments. Hybrid POV systems include aromatic chromophores that can be linked to metals such as Ni, Cu, and Mn. Mixed-metallic and even halogen containing

POV are known, such as the structure $[M(4, 4'\text{-bpy})_2]_2[V^{IV}_7V^V_9O_{38}X] \cdot (4,4'\text{-bpy})_m(H_2O)_n$, where $M = Ni, Co, Mn$; $X = F, Br, Cl$.²¹ POMs such as these, which contain mixed oxidation states, are good conductors of electricity due to their magnetic properties, and as such can perhaps improve conductivity in green energy applications.

The accessible syntheses of the POV through stable intermediates, have provided two significant hybrid structures unique to POV with no corresponding POM analogs.

The first unique POV is an organic-inorganic coordination polymer of the form:

$[M_2(\text{biim})_3V_4O_{12}]$ ($M = Cu, Co$; $\text{biim} = \text{bis-imidazole}$).²² While this does not appear immediately significant, to the best of the author's knowledge, this is the only known hybrid POM composed of only four POM metals. Generally, the smaller the POM, the more charge there is per atom, which makes this structure a highly charge dense POV, and optimal for energy applications. The second POV structure with no similar POM analog is composed of a unique vanadium ring, or callix. This complex features a Ni center, and is capped by another POV, with the formula: $(H_3\text{DETA})_2\{[V^{IV}_{14}V^V_4O_{42} \cdot 2(H_2O)] [Ni(\text{DETA})(\text{HDETA})]_4(H_2O)_6\} [HV^{IV}_{14}V^V_4O_{42}(\text{PO}_4)]$ where $\text{DETA} = \text{diethylenetriamine}$.²³ Circular metal structures like this have been found to exhibit magnetism at the molecular level. Due to the enhancement of electricity by magnetism, utilizing magnetic POM structures to develop conductive materials that also absorb light, are worth investigation in developing alternative materials for green energy applications. It may be suggested that the POV family is the best starting point for building hybrid-lanthanide POMs due to their reliable syntheses, and their known compounds containing transition metals, which may be utilized to link rare-earths.

Despite the range of accessible hybrid POVs compared to the other polyoxometalates, there are no known hybrid-lanthanide-POVs. The known lanthanide-POVs are not coordinated with organic ligands, and have only been recently reported as sandwich-type crystals of the form: $[\text{Ln}(\text{H}_2\text{O})_7]_2[\text{V}_{10}\text{O}_{28}] \cdot 11\text{H}_2\text{O}$, (Ln= Ce , Gd),¹⁹ and the second mixed-nuclear Keggin of the form: $[\{\text{Ln}(\text{H}_2\text{O})_7\}_2\text{As}_6\text{V}_{15}\text{O}_{42}(\text{H}_2\text{O})] \cdot n\text{H}_2\text{O}$; (Ln = La, Sm, Ce).⁹

Lanthanide Polyoxoniobates (PONb)

Polyoniobates (PONb) have the highest charge density of the POMs considered here, which makes them the most desirable POM cluster for the development of energy applications. However, like the POVs there are no known hybrid rare-earth PONb structures. Furthermore, the PONb are fewest in number compared to the other families of POMs. This is mainly due to the high charge density of PONb intermediates, making them stable only in very basic environments. PONb are also regarded as the most difficult to synthesize, being sensitive to reaction conditions, involving water sensitive precursors, and often requiring time-intensive methods and crystal growth rates, such as diffusion of a solvents into an active PONb solutions. It is not surprising that many of the PONb solids are strictly inorganic, being composed in many cases of mixed metals.²⁴⁻²⁶ Indeed the only known PONb coordinated to lanthanides were synthesized by Yamase using high-temperature conditions. These are large and purely inorganic structures with complex lanthanide cores decorated by several hexaniobate clusters.²⁷

A common starting material for PONb systems are the PONb alkali salts developed by Nyman et. al of the form $\text{M}_9\text{Nb}_6\text{O}_{19}$, (M= K, Rb, Cs).²⁸ For example, these hexaniobate precursors have been used by the same group to form PONb composites with

some metal oxides commonly used in solar cells.²⁹ These composites have the forms: $K_{12}[Ti_2O_2][SiNb_{12}O_{40}] \cdot 16H_2O$, and $Na_{14}[H_2Si_4Nb_{16}O_{56}] \cdot 5H_2O$, and represent the potential for PONb to be adapted into known green applications. Additionally, organic cations such as tetramethylammonium may be used in aqueous (hydrothermal) or organic solvent based (solvothermal) reactions to stabilize the hexa- or decaniobate anion.³⁰ Although few PONb systems exploit the use of this starting material, it may be possible with more research on the fundamental properties of hybrid PONb, to coordinate PONb with more elaborate organic dyes, such as those designed to harvest light. These polyconjugated ligands are typically soluble in organic solvents, and realizing new systems including them is likely only to be possible in solvothermal reactions.

There are few known hybrid PONb, and of these clusters, there are none that contain lanthanide atoms. The first series of Cu hybrid PONb was accomplished by Ma et al. by diffusion with nitrogen-containing ligands.³¹ Only recently, the same group reported using hexaniobate alkali precursors in hydrothermal reactions to afford compounds with larger PONb.³² These clusters have the general form of an aromatic nitrogen-containing capping ligand, coordinated to a transition metal, which is then coordinated to the PONb. Interestingly, these structures show the ability to accommodate several different transition metals, which before, had only been Cu and have the form $M(L)_3 \{ [M(L)_2]_2 [Nb_{10}O_{28}] \} \cdot 8H_2O$, (M= Cu, Ni, Co, Zn; L= 1,10 phen. or 2,2 bpy).³²

Very recently, using straightforward hydrothermal methods, the Casey group synthesized a di- transition-metal cored PONb of the form $[Cr_2(OH)_4Nb_{10}O_{30}]^{8-}$ using hydrous Nb_2O_5 .³³ This represents an approach that may be potentially adopted to

accommodate rare-earth atoms through a transition-metal bond. Also, because an organic base was used in this system, it may be possible to incorporate aromatic ligands into this type of PONb using organic solvents. The most remarkable property of this cluster, however, is that it absorbs light in the visible range with no assistance from organic ligands, with peaks around 440 nm and 594 nm (**Figure 1**).

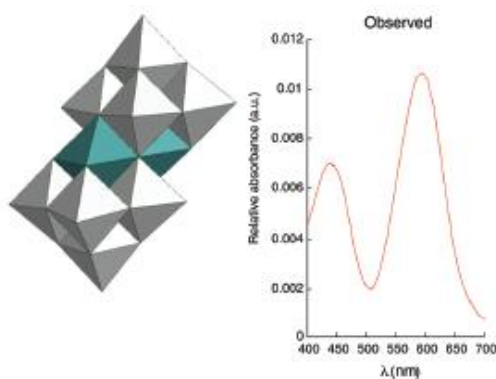


Figure 1. A recent di- transition-metal cored PONb of the form $[\text{Cr}_2(\text{OH})_4\text{Nb}_{10}\text{O}_{30}]^{8-}$. This cluster absorbs in the visible range with no assistance from organic molecules.

The Casey group attributes this interesting visible absorption to Cr^{III} transitions. However, this is one of the only known POMs that exhibits this property, extending the range of PONb significantly. Although computational methods were used and validated by experimental UV spectra, further computational research is needed to explain this phenomenon so that this property may be exploited in the design of new systems.

Computational Methods for POMs

The successful prediction of electronic structures in MOFs, POM coordination polymers, and hybrid lanthanides will allow investigation into the origin of charge transfer in emergent photoactive systems. The fundamental properties of these structures are not entirely understood, and development of computational methods will enable design considerations in realizing an optimized photoactivity.¹ Although some properties,

and transition states of POMs have been calculated, only very recently have the excited states of POMs been predicted by time-dependent density functional theory (TD-DFT), with very good agreement to experimental UV-Vis spectra.³³⁻³⁵ The UV spectra of any system, successfully predicted by TD-DFT, can be used to understand where electron density is transferred within the system upon absorption of light. Generally, each peak in a UV spectra corresponds to a transition from the ground electronic to an excited state. When transition state orbitals are analyzed visually, regions of electron density transfer corresponding to each peak can be shown in sets of pairs from a ground state (hole) to an excited state (particle). This technique is known as natural transition orbital (NTO) analysis, and the pairs representing each peak are known as NTOs or NTO hole-particle pairs.⁷ Also, frequently there may be several NTOs contributing one peak. In these cases, each NTO is assigned a weight based on how much it contributes to the peak.

Basis sets are used in computational chemistry as a kind of electronic map, or starting point for applying predictive calculations to individual atoms in a molecule. For POMS, rather than calculating the interactions between every electron in the system, the heavy atoms, or those with a very large number of electrons like transition metals, typically use basis sets that treat the inner electrons as a pseudopotentials, to conserve computational resources. There are only a few basis sets which support lanthanide atoms, and although the Casey group successfully calculated the excited state spectra of a bi-metallic POM, there are currently no TD-DFT studies on lanthanide-POMs.³³

CHAPTER III TWO ISOSTRUCTURAL LANTHANIDE POLYOXONIOBATES

Outline

This chapter discusses the synthesis and characterization of the compounds $[\text{Dy}_4(\text{H}_2\text{O})_8(\text{SO}_4)_5(\text{NbO}_3)_2] \cdot 3\text{H}_2\text{O}$, and $[\text{Tb}_4(\text{H}_2\text{O})_8(\text{SO}_4)_5(\text{NbO}_3)_2] \cdot 3\text{H}_2\text{O}$. The crystal structures of these solids were determined by single crystal XRD, and results are presented. The solid UV-Vis spectra of these two compounds are very similar, indicating O→Nb, not O→lanthanide centered transitions (verified by TD-DFT in Chapter IV). The solid photoluminescence-emission spectra for both compounds each verify characteristic Dy³⁺, and Tb³⁺ emissions.

Synthesis of $[\text{Dy}_4(\text{H}_2\text{O})_8(\text{SO}_4)_5(\text{NbO}_3)_2] \cdot 3\text{H}_2\text{O}$ (1)

A Solution of $\text{Na}_2\text{S}_2\text{O}_3$ (0.176 mmol), was added to a solution of $\text{K}_2\text{Cr}_2\text{O}_7$ (0.0426 mmol), $\text{Dy}_3(\text{NO}_3)_3$ (0.25 mmol), and H_2O (83.33 mmol), and stirred for 2 minutes at room temperature until becoming slightly dark, and cloudy. Tetramethylammonium hydroxide (TMAOH: $(\text{CH}_3)_4\text{N}(\text{OH})$) (0.550 mmol) was added, and hydrous niobium oxide, $\text{Nb}_2\text{O}_5 \cdot (x\text{H}_2\text{O})$ (0.1337 mmol based on Nb, 0.25 g, 76% w/w) was added to the suspension. The resulting yellow mixture was transferred to a Teflon bag, sealed, and placed in a Teflon-lined steel autoclave. The system was heated to 160° C at 0.72° C/min then kept at 160° C for 18 hrs., and left to cool. Dark pink crystals suitable for single-crystal XRD were separated from light green solids, and separated manually from the remaining pink crystal-like solids. Yield = 5.2%, based on Dy assuming the composition of **1**.

Reacting the system for longer than 18 hours does not seem to improve yield. However, annealing using the same conditions increases yield from 5.2% to 12.2 %,

fewer pink solids are observed, and the overall crystal size is decreased. The reaction proceeds in the pH range of 5.1-6.1 (by adjusting TMAOH), and crystal size is slightly larger at lower pH. The crystals are stable in air and are insoluble in both acidic and basic aqueous solutions, as well as organic solvents (THF, DMF, methanol, ethanol, chloroform, dichloromethane).

Synthesis of $[\text{Tb}_4(\text{H}_2\text{O})_8(\text{SO}_4)_5(\text{NbO}_3)_2] \cdot 3\text{H}_2\text{O}$ (**2**)

$[\text{Tb}_4(\text{H}_2\text{O})_8(\text{SO}_4)_5(\text{NbO}_3)_2] \cdot 3\text{H}_2\text{O}$ (**2**) is prepared using the same conditions as (**1**), except $\text{Tb}_3(\text{NO}_3)_3$ is used instead of $\text{Dy}_3(\text{NO}_3)_3$. Yield = 3.5%, based on Tb assuming the composition of **2**. The crystals are stable in air and are insoluble in both acidic and basic aqueous solutions, as well as organic solvents (THF, DMF, methanol, ethanol, chloroform, dichloromethane).

Structures of $[\text{Dy}_4(\text{H}_2\text{O})_8(\text{SO}_4)_5(\text{NbO}_3)_2] \cdot 3\text{H}_2\text{O}$ and $[\text{Tb}_4(\text{H}_2\text{O})_8(\text{SO}_4)_5(\text{NbO}_3)_2] \cdot 3\text{H}_2\text{O}$

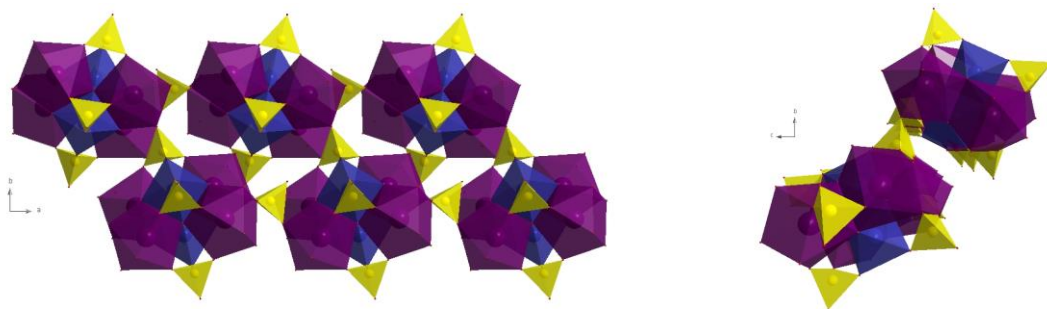


Figure 2. Structure of $\text{Ln}_4(\text{H}_2\text{O})_8(\text{SO}_4)_5(\text{NbO}_3)_2 \cdot 3\text{H}_2\text{O}$, $\text{Ln}=\text{Tb}, \text{Dy}$, shown along the c direction (left), and a direction (right). Purple polyhedra LnO_8 , blue polyhedral NbO_6 , yellow polyhedral SO_4 .

The single crystal XRD structure of the cluster $[\text{Ln}_4(\text{H}_2\text{O})_8(\text{SO}_4)_5(\text{NbO}_3)_2] \cdot 3\text{H}_2\text{O}$; $\text{Ln}=\text{Dy}, \text{Tb}$, is shown in **Figure 2**. The crystal system is monoclinic with the space-group $P2_1$. Lanthanides within the cluster are coordinated to two water molecules. Each lanthanide is bridged by a SO_4^{2-} ion to another lanthanide within the cluster, and SO_4^{2-} ions connect an additional lanthanide along the \mathbf{a} direction to an adjacent cluster, as

shown in **Figure 2**. These clusters are connected by a SO_4^{2-} ion along the c direction, and in this sense the lanthanide niobate cores are linked together, and share six SO_4^{2-} ions.

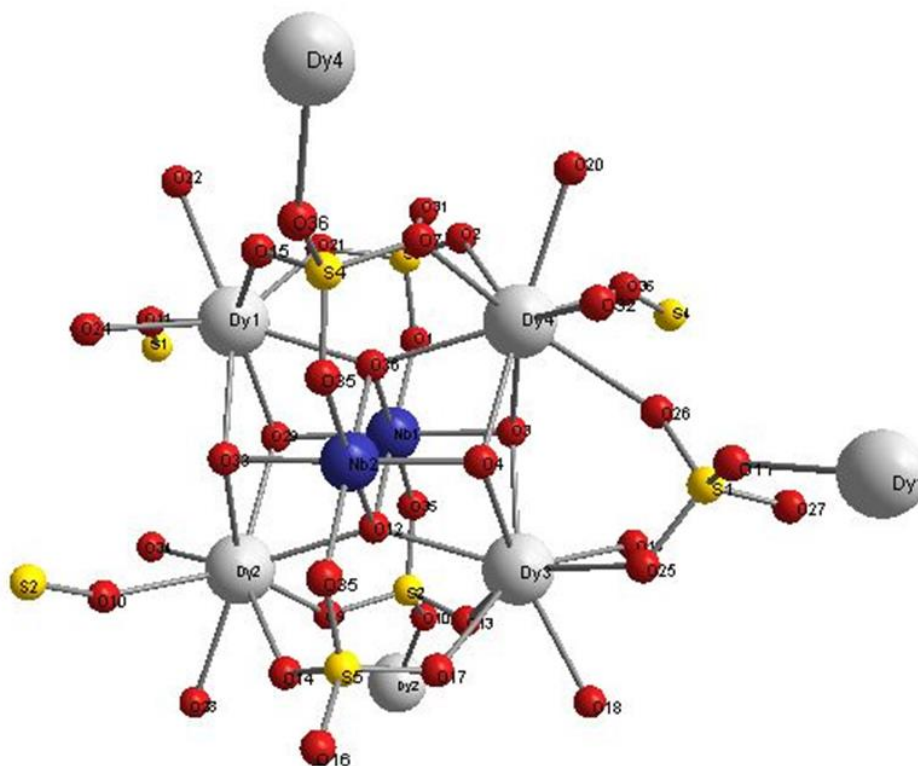


Figure 3. Structure of $[\text{Dy}_4(\text{H}_2\text{O})_8(\text{SO}_4)_5(\text{NbO}_3)_2] \cdot 3\text{H}_2\text{O}$ with extended structure Dy atoms showing connectivity to adjacent clusters through Shared SO_4^{2-} bridges. Repeated atoms are numbered appropriately. Grey spheres Dy, blue spheres Nb, red spheres O, yellow spheres S. Hydrogen atoms are omitted for simplicity. Dy-O (Å) range 2.301-2.435, average =2.301; Nb-O (Å) range 1.931-2.044, average =2.050; S-O (Å) range 1.435-1.502, average 1.470.

The extended structure of $[\text{Dy}_4(\text{H}_2\text{O})_8(\text{SO}_4)_5(\text{NbO}_3)_2] \cdot 3\text{H}_2\text{O}$ represented in **Figure 3** shows SO_4^{2-} ions shared within the Dy-PONb core, and how these SO_4^{2-} ions are shared between adjacent clusters. Crystallographic data and structure refinement for $[\text{Dy}_4(\text{H}_2\text{O})_8(\text{SO}_4)_5(\text{NbO}_3)_2] \cdot 3\text{H}_2\text{O}$ are listed in **Table 1**.

Table 1. Crystallographic data for $[\text{Dy}_4(\text{H}_2\text{O})_8(\text{SO}_4)_5(\text{NbO}_3)_2] \cdot 3\text{H}_2\text{O}$ Crystal data and structure refinement for $[\text{Dy}_4(\text{H}_2\text{O})_8(\text{SO}_4)_5(\text{NbO}_3)_2] \cdot 3\text{H}_2\text{O}$.

Empirical formula	$\text{Dy}_4 \text{Nb}_2 \text{O}_{37} \text{S}_5 \text{OH}_{22}$	
Formula weight	1610.28	
Temperature	295 K	
Wavelength	0.71073 Å	
Crystal system	Monoclinic	
Space group	$P2_1$	
Unit cell dimensions	$a = 10.515(3) \text{ \AA}$	$\alpha = 90^\circ$.
	$b = 12.678(4) \text{ \AA}$	$\beta = 109.634(15)^\circ$.
	$c = 11.824(5) \text{ \AA}$	$\gamma = 90^\circ$.
Volume	$1484.5(9) \text{ \AA}^3$	
Z	2	
Density (calculated)	3.544 Mg/m^3	
Absorption coefficient	11.905 mm^{-1}	
F(000)	1608	
Crystal size	$0.63 \times 0.26 \times 0.20 \text{ mm}^3$	
Theta range for data collection	$1.83 \text{ to } 39.27^\circ$.	
Index ranges	$-15 \leq h \leq 18, -21 \leq k \leq 21, -20 \leq l \leq 20$	
Reflections collected	37018	
Independent reflections	15273 [R(int) = 0.0616]	
Completeness to theta = 39.27°	88.8 %	
Absorption correction	None	
Max. and min. transmission	0.1993 and 0.0498	
Refinement method	Full-matrix least-squares on F^2	
Data / restraints / parameters	15273 / 1 / 421	
Goodness-of-fit on F^2	1.081	
Final R indices [$I > 2\sigma(I)$]	$R1 = 0.0625, wR2 = 0.1721$	
R indices (all data)	$R1 = 0.0629, wR2 = 0.1725$	
Absolute structure parameter	0.635(13)	
Extinction coefficient	0.0050(3)	
Largest diff. peak and hole	$5.469 \text{ and } -12.701 \text{ e. \AA}^{-3}$	

The extended structure of $[\text{Tb}_4(\text{H}_2\text{O})_8(\text{SO}_4)_5(\text{NbO}_3)_2] \cdot 3\text{H}_2\text{O}$ represented in **Figure 4** shows SO_4^{2-} ions shared within the Tb-PONb core. Crystallographic data and structure refinement for $[\text{Tb}_4(\text{H}_2\text{O})_8(\text{SO}_4)_5(\text{NbO}_3)_2] \cdot 3\text{H}_2\text{O}$ is listed in **Table 2**.

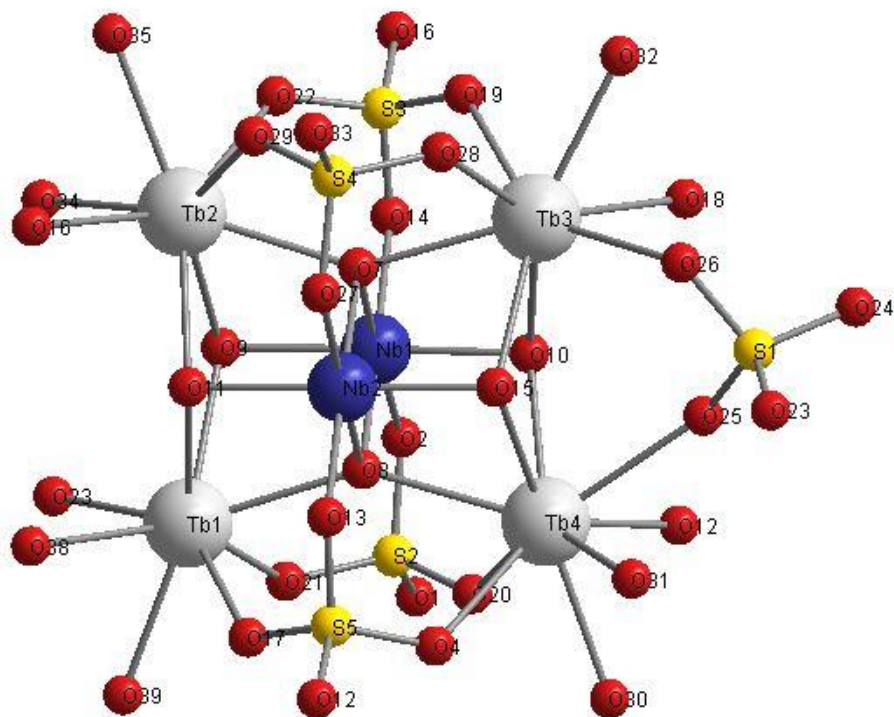


Figure 4. Structure of $[\text{Tb}_4(\text{H}_2\text{O})_8(\text{SO}_4)_5(\text{NbO}_3)_2] \cdot 3\text{H}_2\text{O}$ showing the symmetric unit, and connectivity to adjacent clusters by SO_4^{2-} bridge at O 23. Grey spheres Dy, blue spheres Nb, red spheres O, yellow spheres S. Tb-O (Å) range 2.332-2.446, average =2.405; Nb-O (Å) range 1.932-2.043, average =1.982; S-O (Å) range 1.436-1.507, average 1.473.

Table 2. Crystallographic data for $[\text{Tb}_4(\text{H}_2\text{O})_8(\text{SO}_4)_5(\text{NbO}_3)_2] \cdot 3\text{H}_2\text{O}$.

Empirical formula	$\text{Nb}_2\text{O}_{37} \text{S}_5\text{Tb}_4\text{H}_{22}$	
Formula weight	1595.36	
Temperature	298 K	
Wavelength	0.71073 Å	
Crystal system	$P2_1$	
Space group	monoclinic	
Unit cell dimensions	$a = 10.5680(6)$ Å	$\alpha = 90^\circ$.
	$b = 12.7438(8)$ Å	$\beta = 110.393(2)^\circ$.
	$c = 11.8435(7)$ Å	$\gamma = 90^\circ$.
Volume	$1495.07(15)$ Å ³	
Z	2	
Density (calculated)	2.892 Mg/m ³	
Absorption coefficient	10.484 mm ⁻¹	
F(000)	1164	
Crystal size	0.40 x 0.40 x 0.10 mm ³	
Theta range for data collection	1.83 to 39.17°.	
Index ranges	$-18 \leq h \leq 17$, $-21 \leq k \leq 22$, $-21 \leq l \leq 19$	
Reflections collected	50129	
Independent reflections	15999 [R(int) = 0.0468]	
Completeness to theta = 39.17°	93.9 %	
Max. and min. transmission	0.4204 and 0.1022	
Refinement method	Full-matrix least-squares on F ²	
Data / restraints / parameters	15999 / 1 / 426	
Goodness-of-fit on F ²	0.951	
Final R indices [I > 2σ(I)]	R1 = 0.0692, wR2 = 0.1903	
R indices (all data)	R1 = 0.0695, wR2 = 0.1908	
Absolute structure parameter	0.329(14)	
Extinction coefficient	0.0043(3)	
Largest diff. peak and hole	13.168 and -12.845 e.Å ⁻³	

PXRD of $[\text{Dy}_4(\text{H}_2\text{O})_8(\text{SO}_4)_5(\text{NbO}_3)_2] \cdot 3\text{H}_2\text{O}$ and $[\text{Tb}_4(\text{H}_2\text{O})_8(\text{SO}_4)_5(\text{NbO}_3)_2] \cdot 3\text{H}_2\text{O}$

Simulated powder XRD (PXRD) spectra were calculated with the Diamond crystallographic software package from .cif (crystallographic information format) structure files refined using the ShelX software package. The simulated PXRD spectra of $[\text{Dy}_4(\text{H}_2\text{O})_8(\text{SO}_4)_5(\text{NbO}_3)_2] \cdot 3\text{H}_2\text{O}$ agrees well with the experimental PXRD spectra as shown in **Figure 5**, indicating the solid is highly pure. This purity further supports that experimental electronic spectra correspond to transitions within the solid.

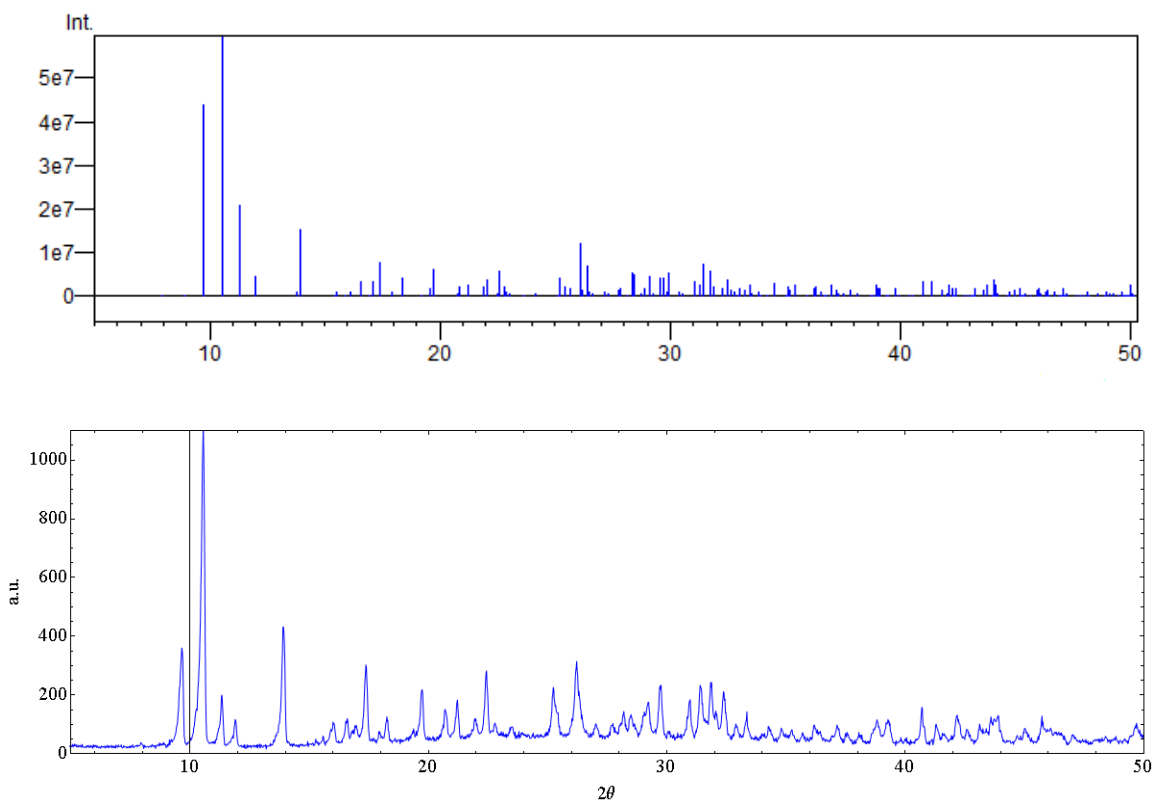


Figure 5. Simulated PXRD (above) and experimental PXRD (below) of $[\text{Dy}_4(\text{H}_2\text{O})_8(\text{SO}_4)_5(\text{NbO}_3)_2] \cdot 3\text{H}_2\text{O}$.

The simulated and experimental PXRD spectra of $[\text{Tb}_4(\text{H}_2\text{O})_8(\text{SO}_4)_5(\text{NbO}_3)_2] \cdot 3\text{H}_2\text{O}$ agrees well with the experimental PXRD spectra as shown in **Figure 6**, indicating this solid is also pure. This purity also supports that

experimental electronic spectra correspond to transitions within the solid, and are likely not attributed to impurities.

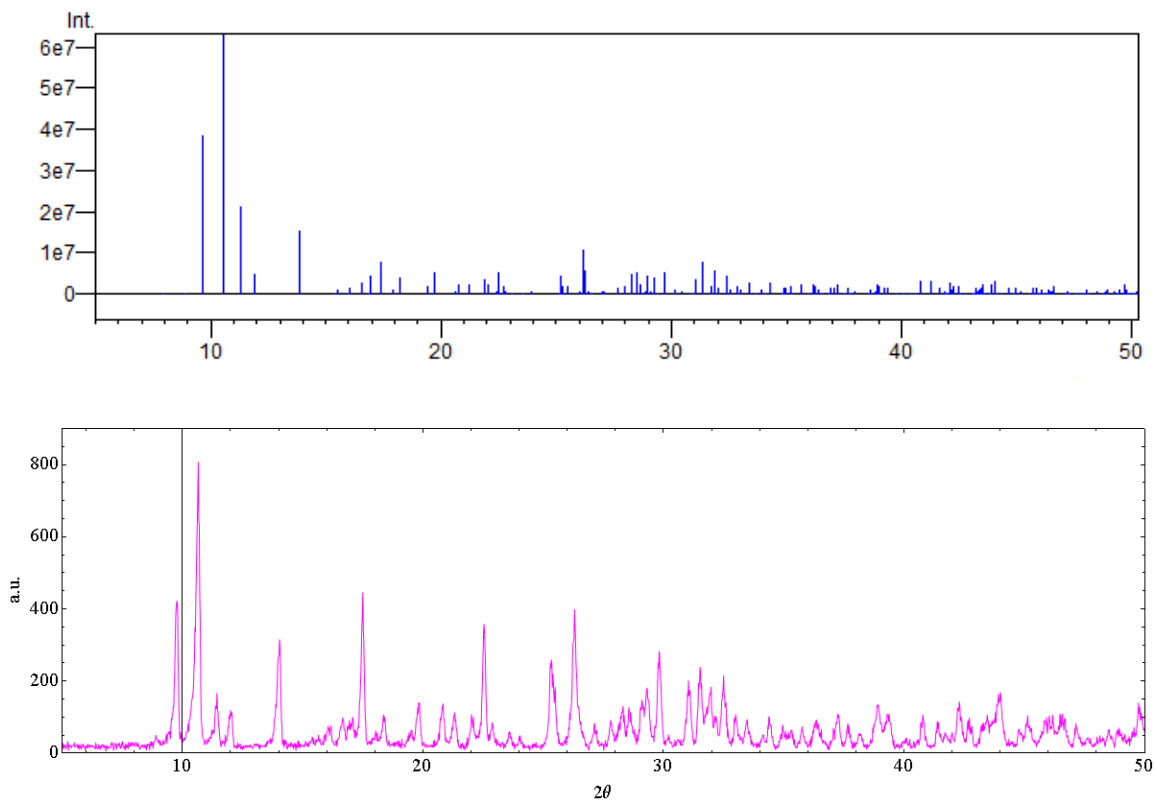


Figure 6. Simulated PXRD (above) and experimental PXRD (below) of $[\text{Tb}_4(\text{H}_2\text{O})_8(\text{SO}_4)_5(\text{NbO}_3)_2] \cdot 3\text{H}_2\text{O}$.

Solid purity could be further confirmed by elemental analysis using electron microscopy techniques such as SEM or TEM.

**Thermal Gravimetric Analysis of $[\text{Dy}_4(\text{H}_2\text{O})_8(\text{SO}_4)_5(\text{NbO}_3)_2] \cdot 3\text{H}_2\text{O}$ and
 $[\text{Tb}_4(\text{H}_2\text{O})_8(\text{SO}_4)_5(\text{NbO}_3)_2] \cdot 3\text{H}_2\text{O}$**

Thermal Gravimetric Analysis (TGA) of $[\text{Ln}_4(\text{H}_2\text{O})_8(\text{SO}_4)_5(\text{NbO}_3)_2] \cdot 3\text{H}_2\text{O}$, (Ln = Dy, Tb) was conducted on a NETZSCH STA 449 F1 Jupiter in nitrogen from 20° C to 750° C at a heating rate of 10° C/ min., and a purge gas flow rate 20 ml/ min. TGA of $[\text{Dy}_4(\text{H}_2\text{O})_8(\text{SO}_4)_5(\text{NbO}_3)_2] \cdot 3\text{H}_2\text{O}$ and $[\text{Tb}_4(\text{H}_2\text{O})_8(\text{SO}_4)_5(\text{NbO}_3)_2] \cdot 3\text{H}_2\text{O}$ is shown in

Figure 7.

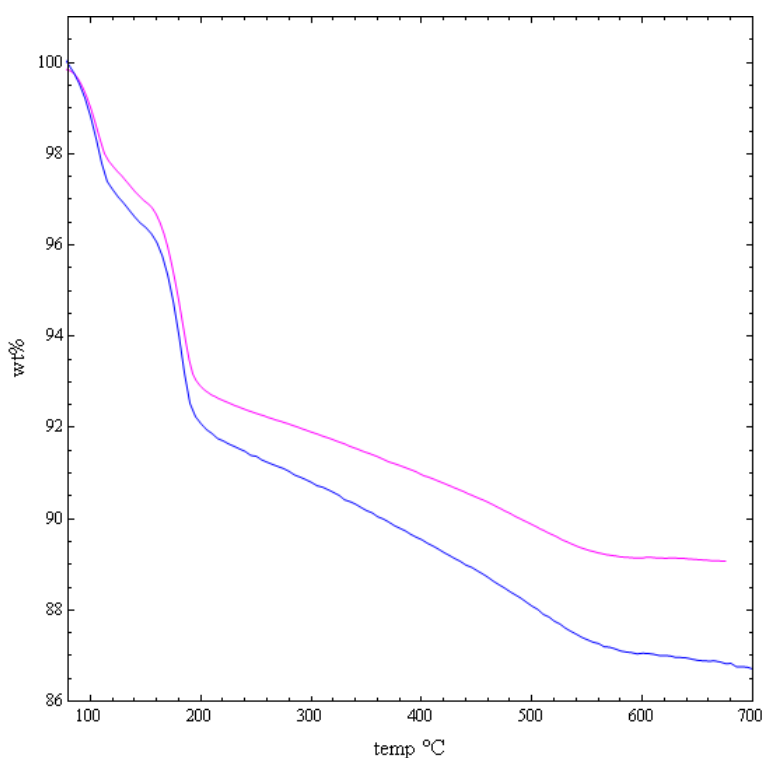


Figure 7. TGA of $[\text{Dy}_4(\text{H}_2\text{O})_8(\text{SO}_4)_5(\text{NbO}_3)_2] \cdot 3\text{H}_2\text{O}$ (blue), and $[\text{Tb}_4(\text{H}_2\text{O})_8(\text{SO}_4)_5(\text{NbO}_3)_2] \cdot 3\text{H}_2\text{O}$ (magenta).

The TGA of both compounds show three regions of weight loss.

$[\text{Dy}_4(\text{H}_2\text{O})_8(\text{SO}_4)_5(\text{NbO}_3)_2] \cdot 3\text{H}_2\text{O}$ has a -3.35% weight loss from 90 °C – 110 °C corresponding to the three lattice water molecules (3.35 wt % calc.), a 5.51% weight loss from 110 °C – 210 °C corresponding to the eight coordinated water molecules (8.94 wt % calc.), and a -5.05% weight loss from 210 °C – 710 °C corresponding to other

combustion products. $[\text{Tb}_4(\text{H}_2\text{O})_8(\text{SO}_4)_5(\text{NbO}_3)_2]\cdot 3\text{H}_2\text{O}$ has a -2.01% weight loss from 90 °C – 110 °C corresponding to the three lattice water molecules (3.39 wt % calc.), a 4.51% weight loss from 110 °C – 210 °C corresponding to the eight coordinated water molecules (9.02 wt % calc.), and a -2.30% weight loss from 210 °C – 680 °C corresponding to other combustion products.

Solid UV-Vis spectra of $[\text{Dy}_4(\text{H}_2\text{O})_8(\text{SO}_4)_5(\text{NbO}_3)_2]\cdot 3\text{H}_2\text{O}$ and $[\text{Tb}_4(\text{H}_2\text{O})_8(\text{SO}_4)_5(\text{NbO}_3)_2]\cdot 3\text{H}_2\text{O}$

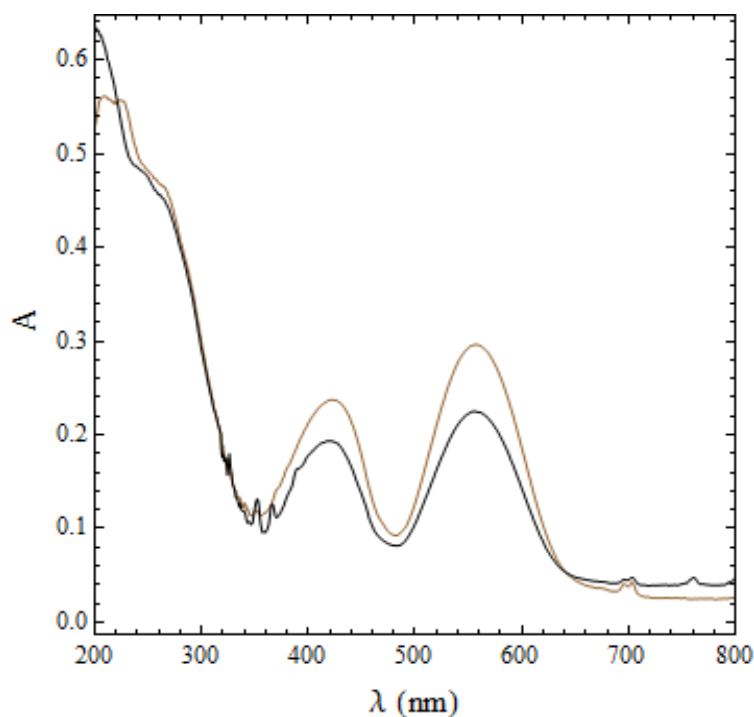


Figure 8. Solid UV-Vis spectra of $[\text{Dy}_4(\text{H}_2\text{O})_8(\text{SO}_4)_5(\text{NbO}_3)_2]\cdot 3\text{H}_2\text{O}$ (black) and $[\text{Tb}_4(\text{H}_2\text{O})_8(\text{SO}_4)_5(\text{NbO}_3)_2]\cdot 3\text{H}_2\text{O}$ (brown).

The solid UV-Vis spectra of $[\text{Dy}_4(\text{H}_2\text{O})_8(\text{SO}_4)_5(\text{NbO}_3)_2]\cdot 3\text{H}_2\text{O}$ and $[\text{Tb}_4(\text{H}_2\text{O})_8(\text{SO}_4)_5(\text{NbO}_3)_2]\cdot 3\text{H}_2\text{O}$ are shown in **Figure 8**. The solid spectra was taken on a Carey 100 Bio SRS-99-010 Spectratron UV-Vis spectrophotometer using double beam mode, with baseline correction. The lamp was changed during the 200-800 nm scan to the

UV lamp at 350 nm. Samples were prepared by layering a dilute methanol suspension of crystals pulverized in a mortar and pestle onto a glass slide. Notably both compounds have two visible absorbances both at 420 nm and 560 nm. This cluster shows visible absorbance unique to polyoxometalates, becoming the second inorganic-POM hybrid with this characteristic absorbance, the first lanthanide POM with this characteristic absorbance, and the first lanthanide PONb.

Solid Luminescence-Emission Spectra of $[\text{Dy}_4(\text{H}_2\text{O})_8(\text{SO}_4)_5(\text{NbO}_3)_2] \cdot 3\text{H}_2\text{O}$ and $[\text{Tb}_4(\text{H}_2\text{O})_8(\text{SO}_4)_5(\text{NbO}_3)_2] \cdot 3\text{H}_2\text{O}$

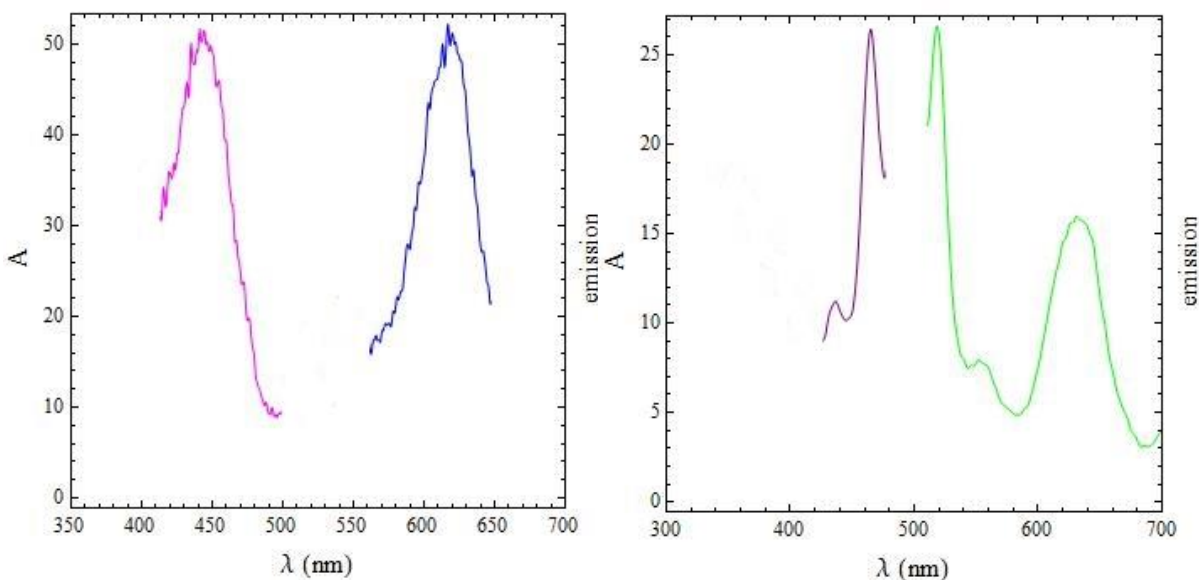


Figure 9. Solid Luminescence-emission spectra of $[\text{Dy}_4(\text{H}_2\text{O})_8(\text{SO}_4)_5(\text{NbO}_3)_2] \cdot 3\text{H}_2\text{O}$ (left) and $[\text{Tb}_4(\text{H}_2\text{O})_8(\text{SO}_4)_5(\text{NbO}_3)_2] \cdot 3\text{H}_2\text{O}$ (right).

The solid luminescence emission spectra of $[\text{Dy}_4(\text{H}_2\text{O})_8(\text{SO}_4)_5(\text{NbO}_3)_2] \cdot 3\text{H}_2\text{O}$ and $[\text{Tb}_4(\text{H}_2\text{O})_8(\text{SO}_4)_5(\text{NbO}_3)_2] \cdot 3\text{H}_2\text{O}$ are shown in **Figure 9**. Samples were prepared in a similar manner to those used in UV-Vis analysis. A Perkin Elmer LS55 Fluorescence Spectrometer was used in scan mode from 250 to 800 nm probe for absorbance and emission wavelengths. Maximum emission wavelengths were then held fixed for each

sample, and their corresponding excitation regions were scanned to determine the maximum excitation wavelength.

As shown in **Figure 9**, two separate lines are represented for each absorbance-emission spectra. The line on the left in each spectra corresponds to the excitation region scanned at the maximum emission wavelength, and the line on the right in each spectra corresponds to the luminescence for each system when excited with the maximum excitation wavelength, which was determined previously and shown on the left.

The Tb^{3+} ion has four distinct luminescence transitions from the $^5\text{D}_4$ orbital. The $\text{Tb}^{3+} \ ^5\text{D}_4 \rightarrow ^7\text{F}_6$ transition corresponds to an emission at 487 nm, the $^5\text{D}_4 \rightarrow ^7\text{F}_5$ corresponds to an emission at 544 nm, the $^5\text{D}_4 \rightarrow ^7\text{F}_4$ corresponds to an emission at 586 nm, and the $^5\text{D}_4 \rightarrow ^7\text{F}_5$ corresponds to an emission at 620 nm.⁴

The Dy^{3+} ion has three distinct luminescence transitions from the $^4\text{F}_{9/2}$ orbital. The $\text{Dy}^{3+} \ ^4\text{F}_{9/2} \rightarrow ^6\text{H}_{15/2}$ transition corresponds to an emission at 493 nm, the $^4\text{F}_{9/2} \rightarrow ^6\text{H}_{13/2}$ corresponds to an emission at 582 nm, and the $^4\text{F}_{9/2} \rightarrow ^6\text{H}_{11/2}$ transition corresponds to an emission at 586 nm. Each solid exhibits characteristic lanthanide luminescence emissions. $[\text{Dy}_4(\text{H}_2\text{O})_8(\text{SO}_4)_5(\text{NbO}_3)_2] \cdot 3\text{H}_2\text{O}$ luminesces at 617 nm at a maximum excitation of 444 nm. $[\text{Tb}_4(\text{H}_2\text{O})_8(\text{SO}_4)_5(\text{NbO}_3)_2] \cdot 3\text{H}_2\text{O}$ luminesces at 518 nm, 552 nm, and 631 nm at a maximum excitation of 476 nm.⁴

CHAPTER IV COMPUTATIONAL METHODS

Outline

This chapter details the computational methods used to calculate electronic structure and spectra for $\text{Dy}_4\text{Nb}_2(\text{SO}_4)_4$. TD-DFT results are in good agreement with the experimental solid $[\text{Dy}_4(\text{H}_2\text{O})_8(\text{SO}_4)_5(\text{NbO}_3)_2]\cdot 3\text{H}_2\text{O}$ spectra, and NTO analysis supports electron transfer corresponding to the main experimental UV-Vis transitions as variations of O \rightarrow Nb ligand to metal charge transfer (LMCT). The development of this approach is described as a series of TD-DFT studies on a calcium MOF, two small organic-lanthanide complexes ($\text{Eu}(\text{COOH})_3$, and $\text{Eu}(\text{NO}_3)_3$), and a theoretical lanthanide-PONb.

Electronic Structure Calculations and Optical Spectra

$\text{Dy}_4\text{Nb}_2(\text{SO}_4)_5$

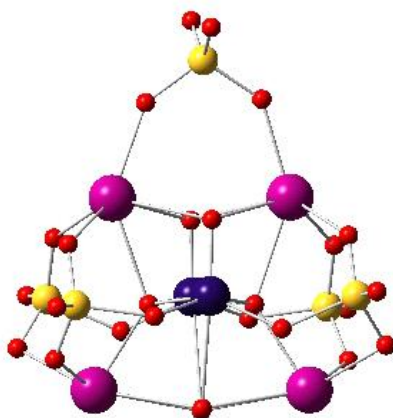


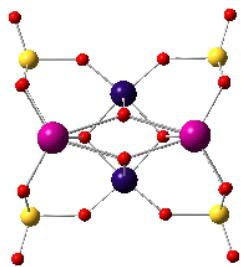
Figure 10. $\text{Dy}_4\text{Nb}_2(\text{SO}_4)_5$ optimized geometry from SXR structure. charge=0, multiplicity=1. PBEPBE/SDD-DF-MWB. purple spheres: Dy; blue spheres: Nb; yellow spheres: S; red spheres: O.

Computational studies were performed using the Gaussian 09 computational chemistry package.³⁶ Water molecules were omitted from the SXR structure for simplicity, and the resulting $\text{Dy}_4\text{Nb}_2(\text{SO}_4)_5$ geometry was optimized at the PBEPBE/SDD-DF-MWB level (**Figure 10**), where the exchange correlation functional

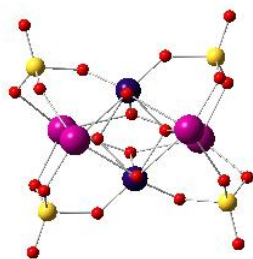
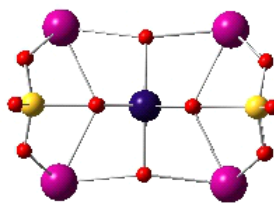
used was that of Perdew, Burke, and Erzenhoff,³⁷ and the Stuttgart-Dresden pseudopotential basis sets used were single-valence-electron Dirac-Fock relativistic (DF) for atoms O and S, and neutral Wood-Boring quasi-relativistic (MWB) for the atoms Nb and Dy (SDD-DF-MWB).³⁸ Normal modes frequency analysis was performed on the optimized $\text{Dy}_4\text{Nb}_2(\text{SO}_4)_5$ geometry, and the structure was confirmed to be a local minimum.

Stability analysis was used to confirm that the singlet wavefunction of the optimized geometry was the ground electronic state. To further confirm the singlet ground state, and also search for possible high-spin ground states that may lead to anti-ferromagnetic coupling, the final optimized $\text{Dy}_4\text{Nb}_2(\text{SO}_4)_5$ singlet geometry was used as the input structure for optimizations of multiplicities 3-19. No lower energy geometries were found for higher multiplicities, indicating a singlet ground state.

$\text{Dy}_4\text{Nb}_2(\text{SO}_4)_4$ TD-DFT Geometries



Geometry A. Optimized $\text{Dy}_4\text{Nb}_2(\text{SO}_4)_4^{2+}$ from SXRD. PE



Geometry B. $\text{Dy}_4\text{Nb}_2(\text{SO}_4)_4$ from optimized $\text{Dy}_4\text{Nb}_2(\text{SO}_4)_4$. PBEPBE/SDD-DF-MWB.

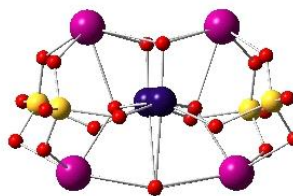


Figure 11. $\text{Dy}_4\text{Nb}_2(\text{SO}_4)_4$ TD-DFT geometries.

TD-DFT was applied to two different $\text{Dy}_4\text{Nb}_2(\text{SO}_4)_4$ geometries (**Figure 11**). The hybrid exchange-correlation functionals PBE/PBE, BP86, and the local M06L exchange-correlation functionals were used in this study.^{37,39,40} The Stuttgart-Dresden basis sets available in Gaussian09 were used for all three functionals.³⁸

Both geometries are generally constructed by omitting the vicinal $(\text{SO}_4)^{2-}$ ion from the $\text{Dy}_4\text{Nb}_2(\text{SO}_4)_5$ cluster. Geometry **A** is the optimized $\text{Dy}_4\text{Nb}_2(\text{SO}_4)_4^{2+}$ cluster from SXRD, and geometry **B** is the $\text{Dy}_4\text{Nb}_2(\text{SO}_4)_4$ cluster taken from the $\text{Dy}_4\text{Nb}_2(\text{SO}_4)_5$ geometry shown in **Figure 10**. The wavefunctions of both geometries **A** and **B** were confirmed to be stable.

Currently, omitting counterions is acceptable in TD-DFT calculations of POMs, although solvation models are typically used to include the influence of a dielectric medium on the electronic structure of the resulting anionic environments.^{33,35} Though the formal charge of the $\text{Dy}_4\text{Nb}_2(\text{SO}_4)_4^{2+}$ is 2, TD-DFT of the neutral geometry **A** (A^0) produces better agreement with the energies and oscillator strengths of the experimental

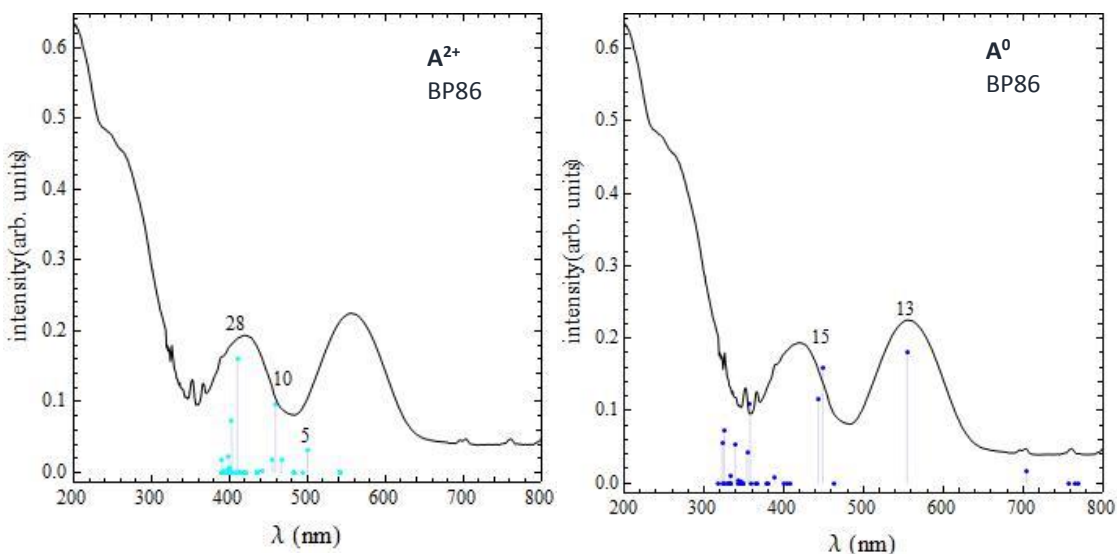


Figure 12. Calculated and experimental spectra of A^{2+} (left) and A^0 (right). BP86/SDD-DF-MWB.

spectra than the formally charged $\text{Dy}_4\text{Nb}_2(\text{SO}_4)_4^{2+}$ (\mathbf{A}^{2+}), **Figure 12**. The experimental high intensity absorbance at 556 nm is not predicted by TD-DFT of the formally charged \mathbf{A}^{2+} geometry vs. TD-DFT of the neutral \mathbf{A}^0 geometry, although the remainder of higher energy transitions between both the $\text{Dy}_4\text{Nb}_2(\text{SO}_4)_4^{2+}$ and $\text{Dy}_4\text{Nb}_2(\text{SO}_4)_4$ geometries are similar.

NTO analysis was performed for \mathbf{A}^{2+} and \mathbf{A}^0 , where 2+ and 0 denote charge. The calculated and experimental spectra of \mathbf{A}^{2+} and \mathbf{A}^0 are shown in **Figure 12**. The calculated spectrum of \mathbf{A}^{2+} consists of three dominant lines at 500, 466, and 413 nm, and agrees with the higher energy peak in the corresponding experimental spectrum, which shows a slight shoulder at 460 nm, and a band at 420 nm. The lower energy transitions of the simulated spectrum have negligible oscillator strengths, and the strong experimental band at 560 nm cannot be determined from this calculation.

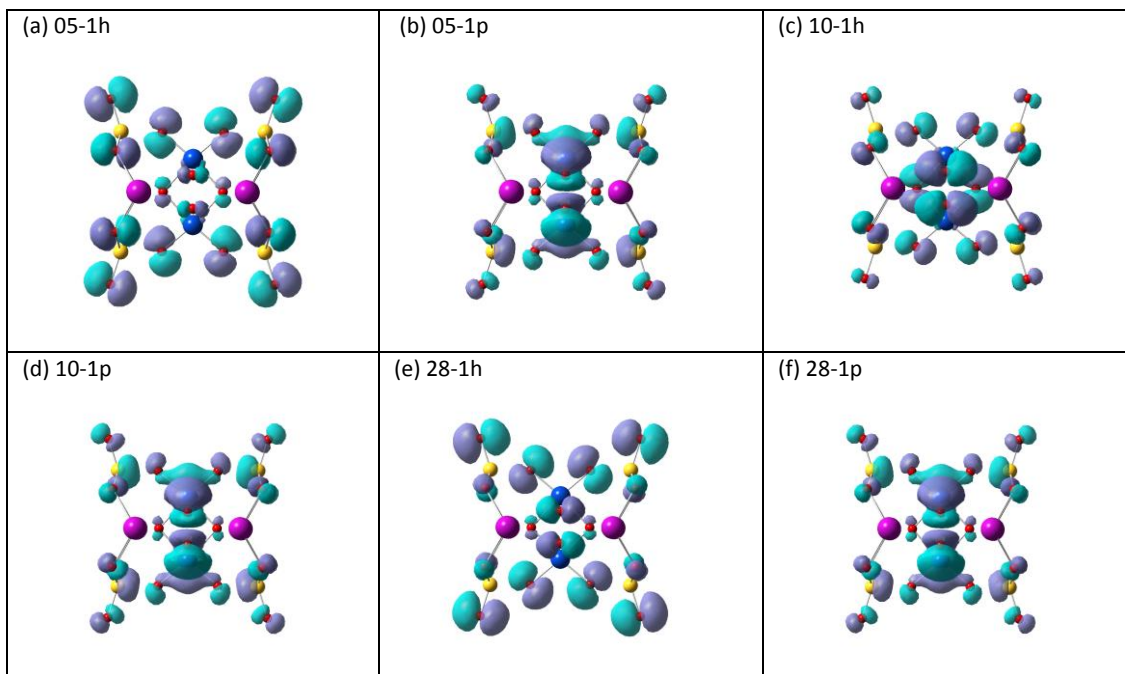


Figure 13. NTO hole/particle pairs for \mathbf{A}^{2+} .

The most significant NTO hole/particle pairs for the A^{2+} transitions are shown in **Figure 13**, and labeled as h or p to denote either a hole or particle, respectively. The highest energy line at 413 nm corresponds to transitions from the ground state to excited state 28. For all NTO pairs, the holes contain a significant contribution from the oxygen atoms, and the corresponding particles all exhibit an anti-bonding pattern within the Nb_2 environment. The holes for NTO pairs 5 and 28 contain mainly contributions from the outer oxygen atoms, while the hole from NTO pair 10 contains more inner oxygen electron density. These transitions are identified as variations of $O \rightarrow Nb$ LMCT.

The calculated spectrum of A^0 (**Figure 12**) consists of two dominant lines at 560, and 454 nm and agrees with the two dominant peaks in the corresponding experimental spectrum, which show bands at 420, and 560 nm. The lower energy transitions of the simulated spectrum have negligible oscillator strengths, but correspond to two very low intensity peaks in the experimental spectra.

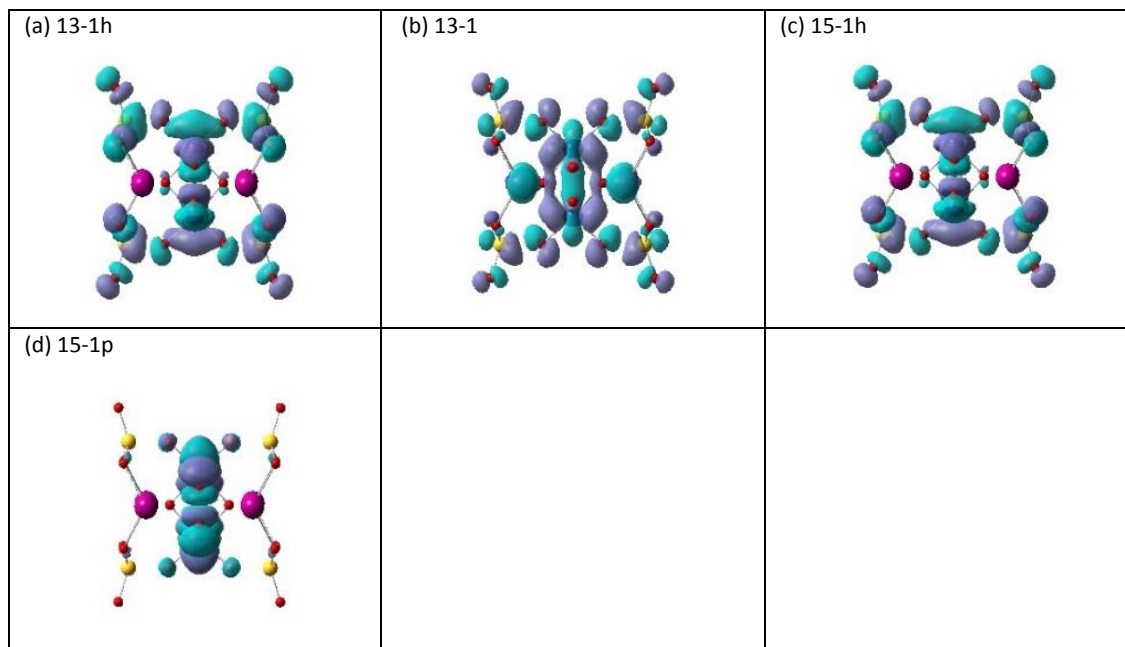


Figure 14. NTO hole/particle pairs for A^0 .

The most significant NTO hole/particle pairs for the \mathbf{A}^0 transitions are shown in **Figure 14**, and labeled as h or p to denote either a hole or particle, respectively. The lines at 560 and 454 nm correspond to transitions from the ground state to excited states 13 and 15, respectively. For both NTO pairs, the holes contain a significant contribution from the oxygen atoms, and the corresponding particles exhibit an anti-bonding pattern within the Nb_2 environment. The holes for NTO pairs 13 and 15 contain mainly contributions from the outer oxygens. The particle for NTO pair 13 has some additional electron density on the outer sulfur and oxygen atoms, while the particle for NTO pair 15 does not. These transitions are identified as variations of $\text{O} \rightarrow \text{Nb}$ LMCT.

As expected due to the removal of electrons from the system, the particles (excited states) of the \mathbf{A}^{2+} geometry look similar to the holes (ground states) of the \mathbf{A}^0 geometry. NTO analysis for both charged and neutral geometry \mathbf{A} , show variations of $\text{O} \rightarrow \text{Nb}$ LMCT. However \mathbf{A}^0 agrees best with the experimental spectra, and the holes for \mathbf{A}^0 have more electron density on oxygen, and less on Nb, than the particles for \mathbf{A}^{2+} .

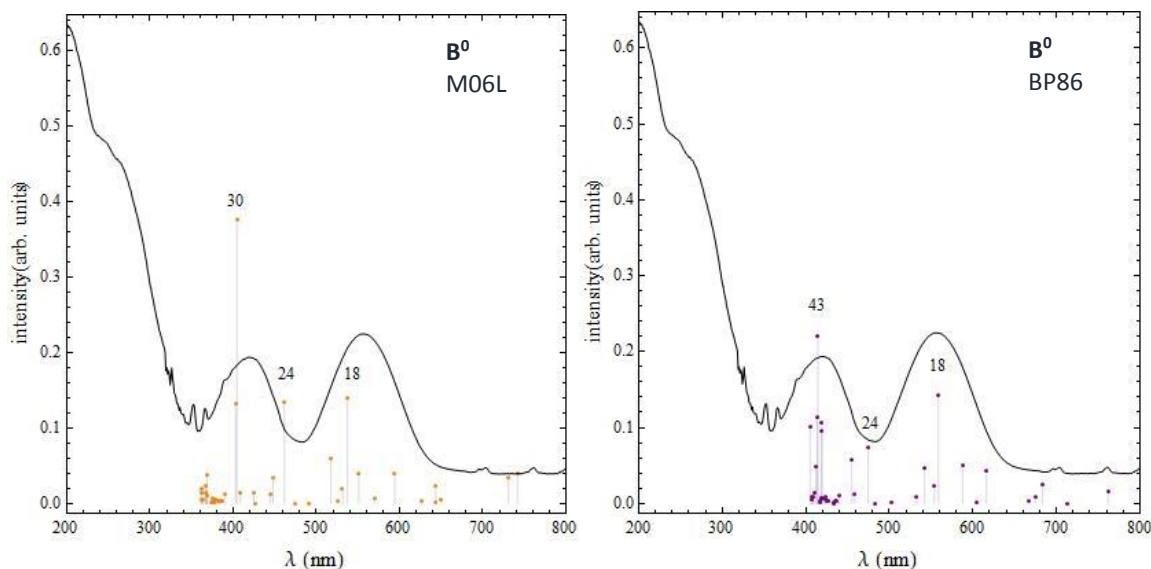


Figure 15. Calculated and experimental spectra of \mathbf{B}^0 . M06L/SDD-DF-MWB. (left) and BP86/SDD-DF-MWB. (right).

The calculated and experimental spectra of \mathbf{B}^0 using the M06L and BP86 exchange-correlation functionals are shown in **Figure 15**. Two functionals were used to validate the \mathbf{B}^0 geometry, and compare estimations of NTO electron density between hybrid and local functionals.

The calculated spectrum of \mathbf{B}^0 M06L consists of three dominant lines at 537, 461, and 405 nm and agrees well with the corresponding experimental spectrum, which shows dominant bands at 420, and 560 nm, and a slight shoulder at 460 nm.

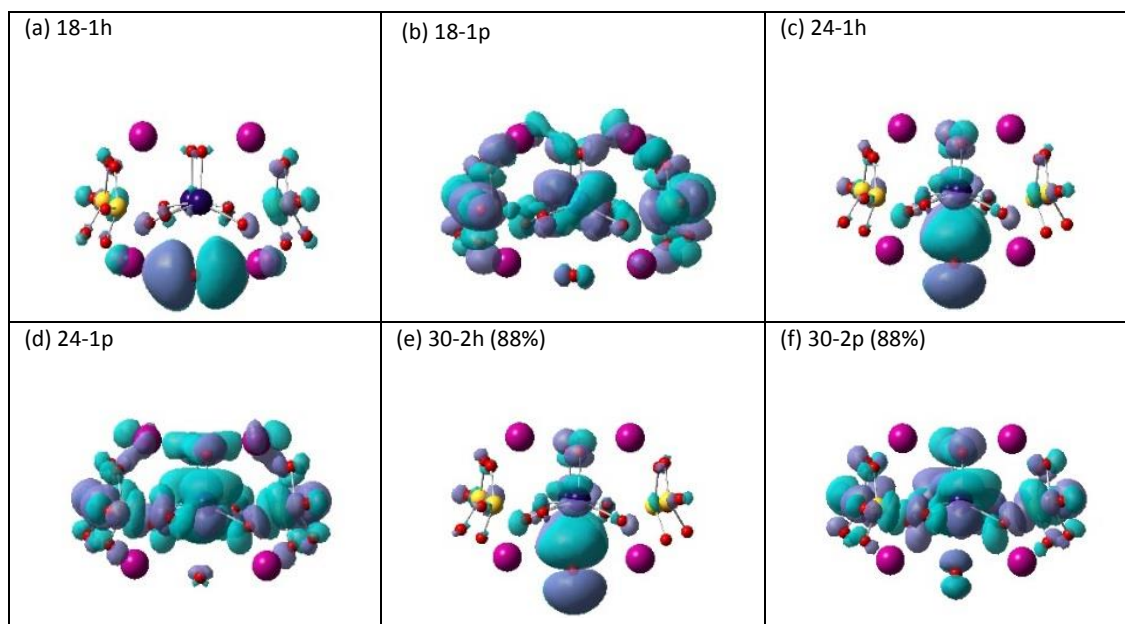


Figure 16. NTO hole/particle pairs for \mathbf{B}^0 M06L.

The most significant NTO hole/particle pairs for the \mathbf{B}^0 M06L transitions are shown in **Figure 16**, and labeled as h or p to denote either a hole or particle, respectively. The lines at 537, 461, and 405 nm correspond to transitions from the ground state to excited states 18, 24, and 30 respectively (**Figure 13**). For all NTO pairs, the holes contain a significant contribution from an oxygen nonbonding lone pair p, or π bonding orbital, and the corresponding particles all exhibit an anti-bonding pattern within the Nb_2

environment. Similar to \mathbf{A}^0 , the particle for NTO pair 18 shows outer sulfur and oxygen electron density in addition to the Nb₂ centered antibonding pattern, and the particles for NTO pairs 24 and 30 also show increasingly less contribution from the outer oxygen and sulfur than atoms the lower energy transition 18. These three transitions are identified as variations of O→Nb LMCT.

The calculated spectrum of $\mathbf{B}^0 \mathbf{BP86}$ (**Figure 12**) consists of two dominant lines at 559 and 414 nm and agrees with the two dominant peaks in the corresponding experimental spectrum, which show strong bands at 420 and 560 nm.

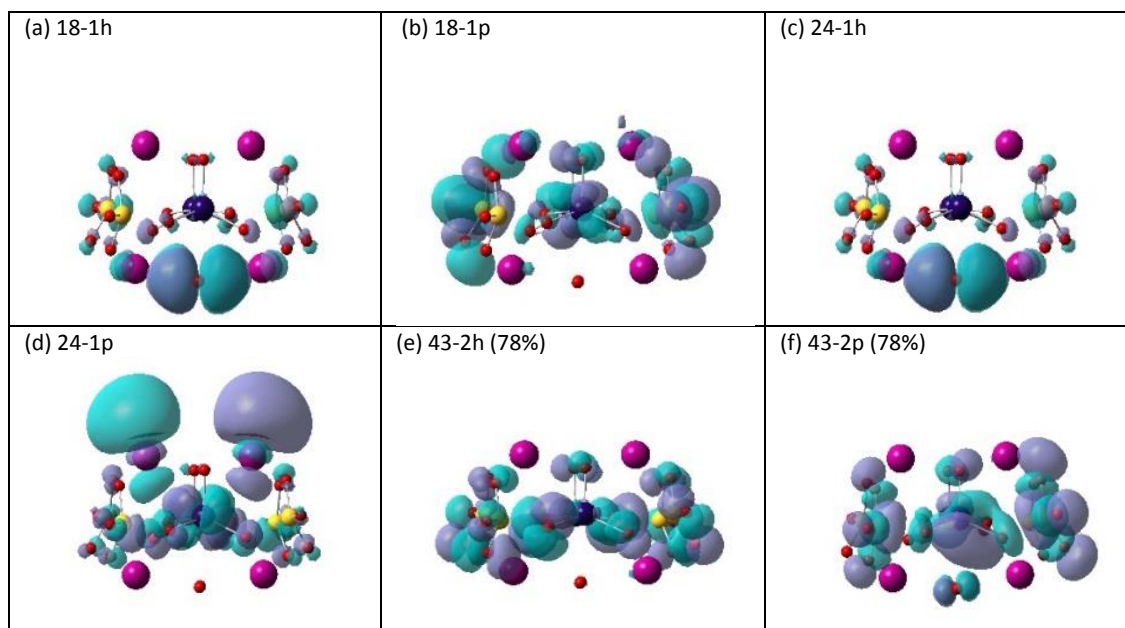


Figure 17. NTO hole/particle pairs for $\mathbf{B}^0 \mathbf{BP86}$.

The most significant NTO hole/particle pairs for the $\mathbf{B}^0 \mathbf{BP86}$ transitions are shown in **Figure 17**, and labeled as h or p to denote either a hole or particle, respectively. The lines at 559 and 414 nm correspond to transitions from the ground state to excited states 18 and 43 respectively. For all NTO pairs, the holes contain a significant contribution from an oxygen π bonding orbital, and the corresponding particles all exhibit an anti-bonding pattern within the Nb₂ environment. Similar to \mathbf{A}^0 , and $\mathbf{B}^0 \mathbf{M06L}$, the

particle for NTO pair 18 shows outer sulfur and oxygen electron density in addition to the Nb₂ centered antibonding pattern, and the particles for NTO pairs 24 and 43 also show less contribution from the outer oxygen and sulfur than atoms the lower energy transition 18. The BP86 functional calculates electron density on two of the Dy atoms for the particle of state 24. These two Dy atoms are bridged by an SO₄²⁻ ion in the crystal structure, and for particles like this predicted by the hybrid functionals, it is likely that electron density is delocalized by the SO₄²⁻ bridge in the crystal structure. These three transitions are identified as variations of O→Nb LMCT.

The constrained geometry **A**, is similar to the crystal structure, and has NTO hole-particle pairs that are more symmetric and more clearly defined than those of the less constrained geometry **B**. Using two geometries for the neutral Dy₄Nb₂(SO₄)₄, and both hybrid and local functionals to account for differences in how electron density is estimated in some of the excited states, the major experimental transitions are validated generally as variations of O→Nb, LMCT. This is expected as the cluster is isostructural (Dy can be replaced by Tb), and the Tb₄Nb₂(SO₄)₅ experimental solid spectra has the same absorbances as the Dy₄Nb₂(SO₄)₅ (**Figure 8.**).

Notably the hybrid exchange-correlation functionals predict Dy electron density in some of the NTO particles of the **A**⁰ and **B**⁰ geometries to a greater degree than the local M06L exchange-correlation functional. This is evident in the particle of NTO pair 15 for geometry **B**⁰ **BP86** (**Figure 15**) and the particles of NTO pair 13 for geometry **A**⁰, shown in **Figure 18**.

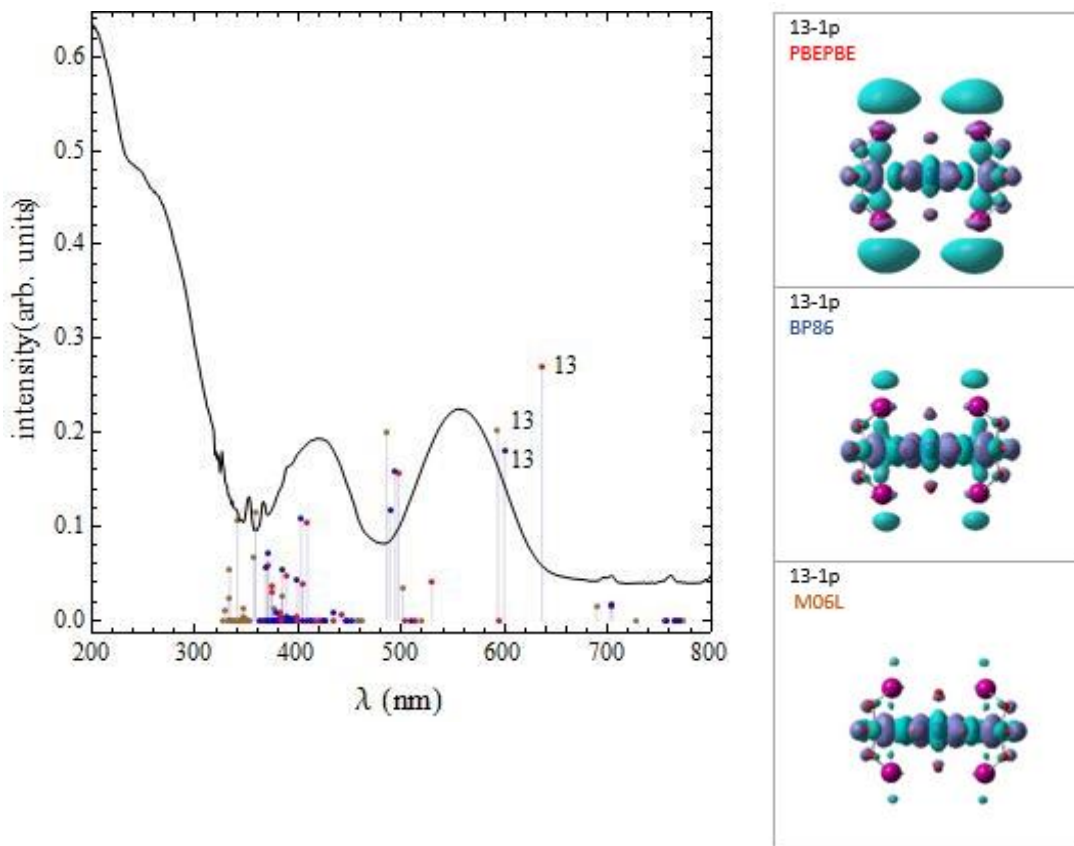


Figure 18. TD-DFT of geometry A^0 , $Dy_4Nb_2(SO_4)_4$ with different functionals. red: PBEPBE, blue: BP86, brown: M06L. (right), and NTO particles for state 13, geometry A^0 , with different functionals (left).

The large density of states for geometry A^0 around 400nm using the PBEPBE, BP86, and M06L functionals, correspond to UV transitions. Because of this, the final spectra of A^0 , using BP86 (as shown in **Figure 12.**) was blue-shifted 40 nm. As mentioned, the hybrid exchange-correlation functionals estimate electron density on the Dy atoms for some of the A^0 and B^0 particles to a greater extent than the local M06L functional. Examples of decreasing electron density for a Dy in an NTO particle are shown in **Figure 16.**—the A^0 particles for NTO pairs 13 using PBEPBE (red), BP86 (blue), and M06L (orange). This, as well as particle 24 for B^0 BP86 (**Figure 17.**), is ultimately why M06L was selected as the method of choice.

CHAPTER V CONCLUSIONS

Outline

This chapter summarizes the synthetic and computational results of this project. The synthetic, and spectroscopic significance of the $[\text{Ln}_4(\text{H}_2\text{O})_8(\text{SO}_4)_5(\text{NbO}_3)_2] \cdot 3\text{H}_2\text{O}$; Ln = Dy, Tb system to the field of POM, and PONb chemistry is discussed and summarized. The computational method applied to the $\text{Ca}_2\text{-btc-pzc}$ MOF, and the computational method developed to accommodate lanthanides in transition metal-oxide clusters is also summarized and discussed.

Summary

Nb clusters offer a charge environment unique to POM clusters. The charge densities per PONb atom in these systems are high due to the Nb (V) oxidation state, and represent a rich electron source for new electronically active POM applications, that may lead to improved conductive properties. Some heterometallic PONbs have been recently synthesized that exhibit the unique property of visible, red-shifted absorbance. The the $[\text{Ln}_4(\text{H}_2\text{O})_8(\text{SO}_4)_5(\text{NbO}_3)_2] \cdot 3\text{H}_2\text{O}$; Ln = Dy, Tb system is the second known PONb cluster to exhibit this property, and the first lanthanide PONb. Though the mechanisms of this synthesis are not clear, this represents the first acidic PONb workup, providing an approach that may be adapted for the development of new PONb.

Although charge lifetimes in lanthanide POMs have not been studied, the absorbance and luminescence properties of the the $[\text{Ln}_4(\text{H}_2\text{O})_8(\text{SO}_4)_5(\text{NbO}_3)_2] \cdot 3\text{H}_2\text{O}$; Ln = Dy, Tb system are significant to photoactive POM chemistry because they represent a charge dense electron source with a lowered absorbance energy, that due to the known

property of long charge lifetimes in *f*-orbital containing systems, may not have the direct consequence of a shortened charge lifetime, that typically occurs when the band gap is lowered.

There are relatively few computational methods used for POM and MOF solids, and the development of methods for organic-inorganic frameworks, and heterometallic lanthanide systems will enable the investigation of properties such as electron-transfer, spin effects, bonding, and synthetic mechanisms in emerging solids. Although a coordination environment for the Ca₂-btc-pzc compound that included Ca²⁺ ions was not found that conclusively predicted the electronic spectra, the main experimental transitions of this MOF can be identified by applying TD-DFT and NTO analysis to the free ligands. Furthermore, the Stuttgart-Dresden pseudopotential basis sets were used in DFT, and TD-DFT studies to predict the electronic spectra of some small lanthanide hybrids, as well as heterometallic lanthanide clusters. NTO analysis of the Dy₄(Nb₂O₆)(SO₄)₄ system represents the first NTO analysis of a lanthanide POM, and using SDD basis sets for these systems represent a straightforward, reliable approach that is relatively non-demanding on computational resources, and can be used in NTO analysis.

APPENDIX A

COMPUTATIONAL TERMS

Density functional theory

Density functional theory (DFT) is a computational approach for determining the energy of a molecular system by solving the Kohn-Sham equations, where the total electronic energy is a functional of the ground-state electron density. The Kohn-Sham orbitals are then non-interacting single electron wavefunctions; in other words, each Kohn-Sham orbital is an eigenstate of a single potential that is not explicitly dependent on the other electrons. In DFT, the wavefunction is a single Slater determinant of orbitals, and is used to calculate the electron density. The approach of DFT is to determine a charge density and obtain successively better approximations to that charge density by adjusting variational parameters (i.e., the Kohn-Sham molecular orbital coefficients). The ground state correlation energy is approximated with the exchange, as a functional of the orbitals- and is called the exchange-correlation functional. In DFT, when the total energy of the system is minimized with respect to variational parameters, the resulting one-particle equations are the same as those in the Hartree-Fock method (except for how electron exchange correlation is incorporated).

Hartree-Fock exchange, often referred to as *ab initio*, is evaluated on all of the Hartree-Fock orbitals of the system, an exact Hamiltonian is assumed to obtain successively better approximations of the wavefunction, and additional methods, such as MP2, are often used to incorporate correlation energy. DFT results are similar to those obtained from *ab initio* methods, but due to the correlation being inherently included, at a significantly reduced computational cost.⁷⁷

Geometry optimizations and normal mode frequency analysis

Geometry optimizations find transition state geometries by locating extrema on the potential energy surface of a molecular system. The minimum energy geometry is typically used to model the UV-Vis spectra, because we assume that most molecules will be close to the equilibrium geometry. As temperature increases spectral peaks broaden. One reason for this is that the molecular ensemble is distributed over more geometries in the ground state. A geometry optimization is successful when a point on the potential energy surface (typically a minimum) is found; i.e. the convergence criteria is met, or the forces are zero and the next step is very small. However, molecules with several torsional degrees of freedom such as alkanes, may have a range of geometries which based on the cutoff criteria are equivalent to the minimum. In these cases, cutoff criteria such as step size, displacement, maximum force, and root-mean-square force may need to be adjusted to find an acceptable stationary point, or different starting geometries may need to be used. At a stationary point, it is typical for normal mode frequency analysis to be conducted in order to verify that a local minimum has been obtained. Normal mode analysis, often referred to as frequency calculations, determine the normal modes of vibration for a system, and thus can be used to predict IR spectra. If there are any imaginary frequencies in the predicted spectra of an equilibrium geometry, the structure is not a local minimum and convergence criteria may need to be adjusted.^{78,79}

Time-dependent density functional theory

Time-dependent density-functional theory (TD-DFT) extends the ideas of ground-state DFT to the treatment of the time-dependent Schrodinger equation. In TD-DFT the exchange-correlation potential is used to calculate the ground-state electron density with

respect to time, the initial wavefunction, and the initial Kohn-Sham wavefunction. Based on the strength of the time-dependent Kohn-Sham potential, it may be used to describe strong field phenomena, such as systems in laser fields,⁸⁰ or weak field phenomena, such as the UV-Vis spectra of a system. When a molecular system is excited, the density rearranges in response to the applied field. In terms of single excitations of the system, once a molecular structure is known, a Fourier-transform of the time-dependent dipole matrix hence yields the optical spectrum- the eigenvalues correspond to transition frequencies or energies, and the eigenvectors produce oscillator strengths.

Natural Transition Orbital Analysis

Natural transition orbital (NTO) analysis is used to characterize electronically excited states. When an excited state, or TD-DFT spectrum is calculated, electronic transitions may be represented as a molecular picture: an ensemble of excitations where each has a ground state energy and intensity corresponding to the promotion of an electron from a single occupied molecular orbital to a single unoccupied one. However, this singular molecular orbital electronic transition description is typically only appropriate for the HOMO-LUMO transition; this is known as Koopman's theorem. In actuality there may be several electronic promotions from occupied to unoccupied states which make up a transition or amplitude. For these transitions, NTO analysis provides a mathematical means to transform all of the molecular orbitals contributing to an excitation, into a smaller set of weighted "NTO hole-particle pairs." For an electronic transition, the NTO holes represent vacant regions of charge density upon excitation, and the NTO particles represent regions of space that are filled after the charge density

rearranges. Often, graphical representations of NTO hole-particle pairs correspond to chemically intuitive regions of electron density transfer, and may be used to describe the nature of electronic transitions.⁷

APPENDIX B

Development of Computational Methods

Calcium Metal Organic Frameworks

Some studies on magnesium and calcium have been reported previously,⁴³ and recent studies have shown that doping alkaline earth metals or alkaline metals in MOFs may enhance their ability for gas storage due to the stronger binding capability of these metals to certain gases such as CO₂ or H₂.^{44,45} The assembly of MOFs from calcium and polycarboxylate linkers, including aliphatic or aromatic carboxylate ligands, is receiving increased interest due to their flexibility as multidentate ligands.⁴⁶⁻⁵³

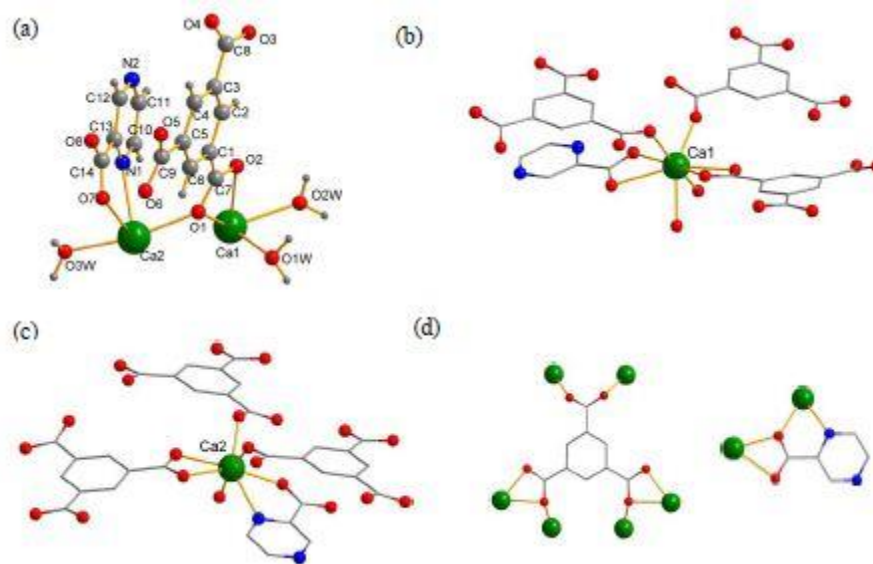


Figure 19. (a) The asymmetric unit; (b) the coordination environment of Ca; (c) the coordination environment of Ca; (d) the coordination environment of the btc and pzc ligands in compound 1.

A crystalline alkaline earth metal coordination polymer phase, [Ca₂(btc)(pzc)(H₂O)₃] (**1**) was synthesized by Yan and co-workers⁵⁴ and is represented in **Figure 19**. Electronic structure calculations using density functional theory (DFT) methods³⁶ were performed on the hydrated and ionic free ligands, as well as on various truncations of the coordination environment derived from the experimental SXRD crystal

structure. The free ligand excited state calculations were in good agreement with the experimental UV-Vis spectra. Coordination environments, which included the calcium atom itself, or the calcium represented as a static 2+ charge, were not in good agreement with the experimental spectra. However, the basis sets and exchange correlation functionals used during these attempts provided direction into the development of a computational approach for metal-organic hybrid structures.

Free acids (H₃btc and Hpzc) and ions (btc and pzc) in water

Geometry optimizations were performed to obtain gas phase minima of the free H₃btc and Hpzc acids, and the btc (-3) and pzc (-1) anions. These calculations were carried out using the PBE/PBE/cc-pVDZ model chemistry^{37, 55} and a normal modes frequency analysis was used to confirm that the final structures were local minima. To model the effects of an implicit water solvent, geometry optimizations and frequency calculations were carried out for all species using a self-consistent reaction field (SCRF).⁵⁶ Finally, the electronic transitions of the solvated species were calculated using the TD-DFT⁵⁷⁻⁶³ method and the dominant transitions were examined using natural transition orbital (NTO) analysis. The results of these calculations are in good agreement with the experimental UV spectrum of H₃btc and Hpzc in aqueous solution.

H₃btc in water

The calculated and experimental spectra of H₃btc in water are shown in **Figure 20**. The calculated spectrum consists of four dominant lines at 253, 242, 229, and 217 nm and agrees well with the corresponding experimental spectrum, which shows a band at 209 nm and a shoulder at 238 nm. The lower energy transitions of the simulated

spectrum have negligible oscillator strengths, and the very weak experimental band at 294 nm cannot be determined from this calculation.

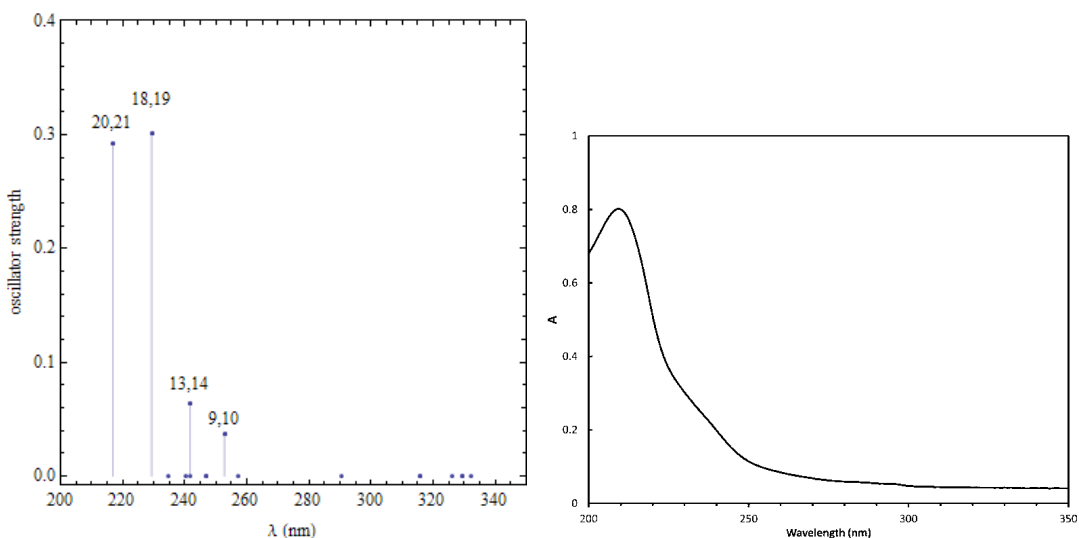


Figure 20. Calculated (left) and experimental (right) UV spectra of H₃btc in water.

The most significant NTO hole/particle pairs for these transitions are shown in **Figure 21**, and labeled as h or p to denote either a hole or particle, respectively. The lowest energy line at 253 nm corresponds to transitions from the ground state to excited states 9 and 10. The first NTO pair of both states represents 28% of the electronic transition, while the second pair is the more dominant contribution with a weight of 72%. For all NTO pairs, the holes contain a significant contribution from the carbon-oxygen π bond, and the corresponding particles all clearly exhibit a π^* anti-bonding pattern within the phenyl ring. Although hydroxyl group electron density contributions are non-bonding, the transitions for this spectral line are identified as $\pi \rightarrow \pi^*$, and also involve some charge transfer from the carboxylic acid groups to the phenyl ring.

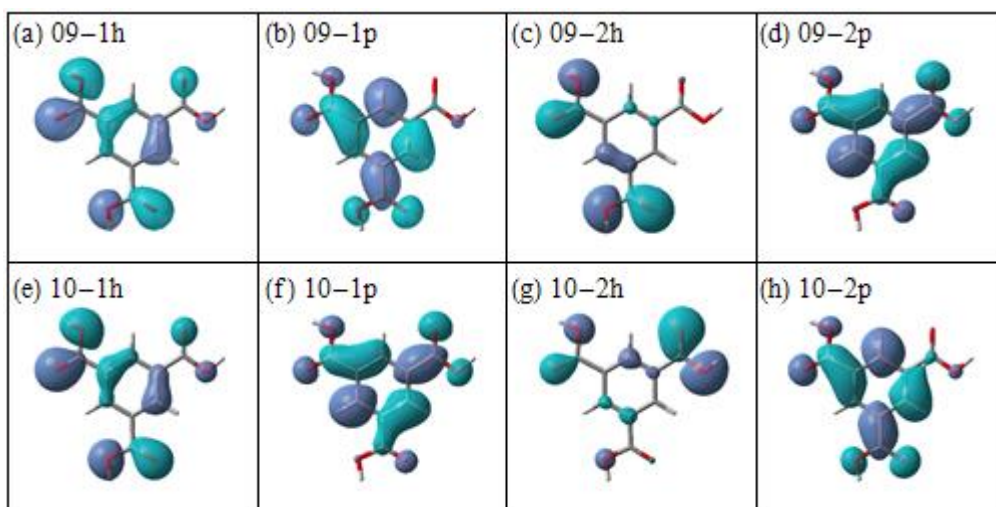


Figure 21. NTO hole/particle pairs for the calculated electronic transitions of H3btc at 253 nm.

The next line at 242 nm corresponds to transitions from the ground state to excited states 13 and 14. The NTO hole/particle pairs for these transitions are shown in **Figure 22**. Similar to the previous transitions, the contributions made by NTO pairs 1 and 2 are 27% and 68%, respectively, for state 13 and 29% and 66%, respectively, for state 14. The NTO holes consist of both n-type character on the hydroxyl oxygen atoms and π bonding within carbonyl groups; however, there is more contribution from carbon-carbon π bonds within the phenyl ring. These transitions are classified as $\pi \rightarrow \pi^*$ type transitions.

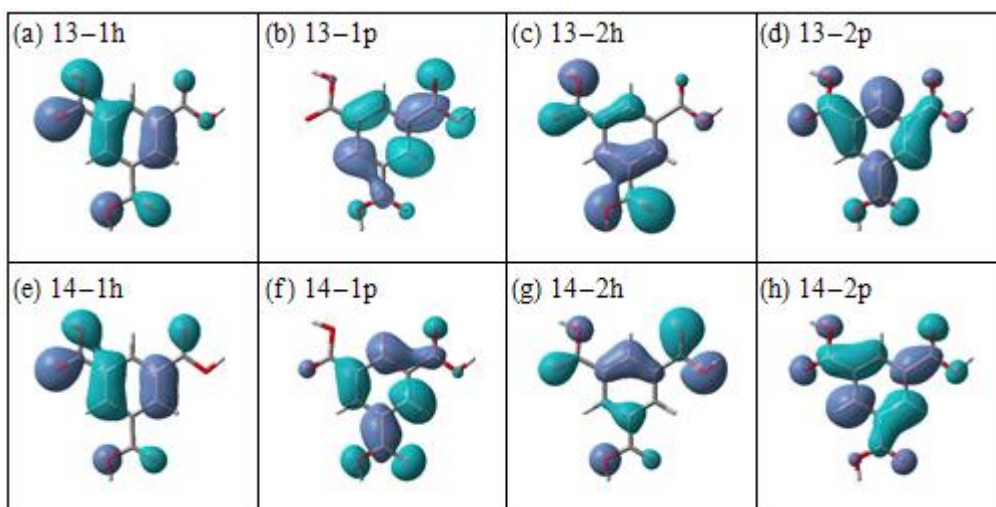


Figure 22. NTO hole/particle pairs for the calculated electronic transitions of H₃btc at 242 nm.

The spectral line at 229 nm corresponds to transitions to states 18 and 19. The NTO hole/particle pairs for these transitions are shown in **Figure 23**. Again, there are two dominant NTO pairs for each transition; however, the weights are more or less equal: 45% and 47% for state 18 and 44% and 49% for 19. For both transitions, the NTO holes exhibit a very clear π bonding pattern within the phenyl ring and the NTO particles have π^* anti-bonding character. These are classified as $\pi \rightarrow \pi^*$ transitions.

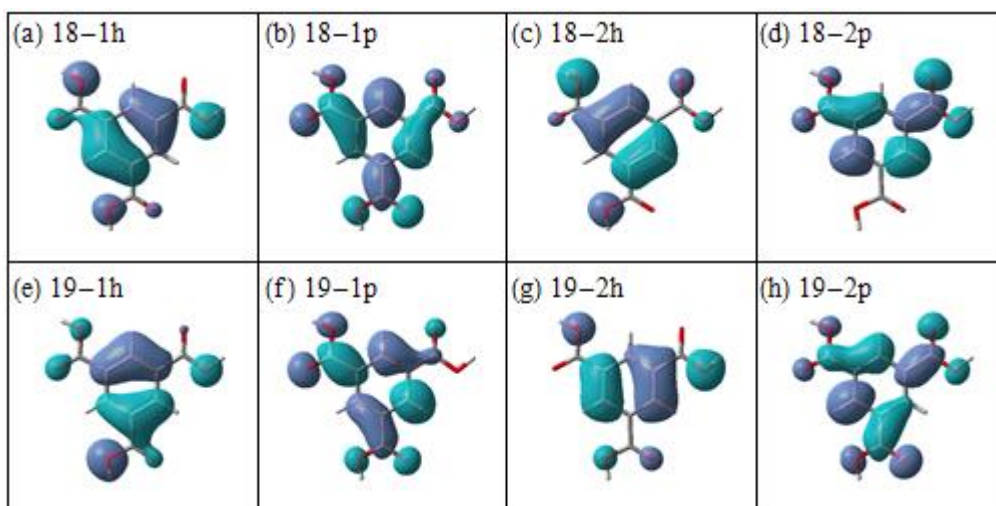


Figure 23. NTO hole/particle pairs for the calculated electronic transitions of H₃btc at 229 nm.

The highest energy line at 217 nm corresponds to transitions from the ground state to states 20 and 21, and the NTO hole/particle pairs are shown **Figure 24**. There is only one dominant pair for state 20, and it has a weight of 87% (all other NTO pairs all have weights less than 10%). For state 21, there are two NTO pairs with weights greater than 10%. The first NTO pair represents 11% of the transition, and the second pair contributes 87%. For both state 20 and 21, the dominant NTO pairs are consistent with $\pi \rightarrow \pi^*$ transitions; however, there are clearly more nodes in the NTO particle, which would correspond to a higher energy π^* orbital.

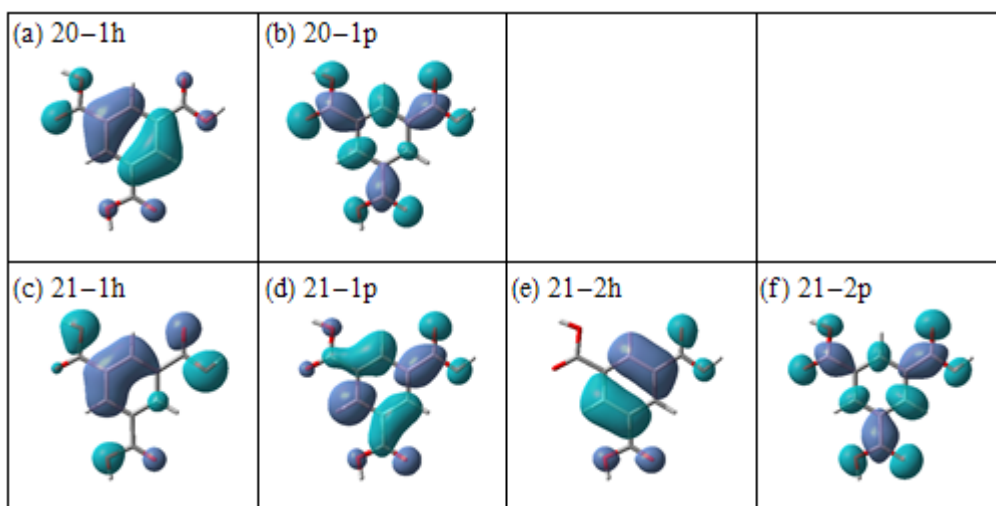


Figure 24. NTO hole/particle pairs for the calculated electronic transitions of H3btc at 217 nm.

Hpzc in water

The simulated and experimental spectra of Hpzc in water are shown in **Figure 25**. There are two dominant spectral lines in the calculated spectrum at 254 and 219 nm, and these transitions are associated with the observed bands at 268 nm and 205 nm in the experimental UV spectra of Hpzc in water. From this calculation we are not able to identify an electronic transition corresponding to the observed band at 312 nm.

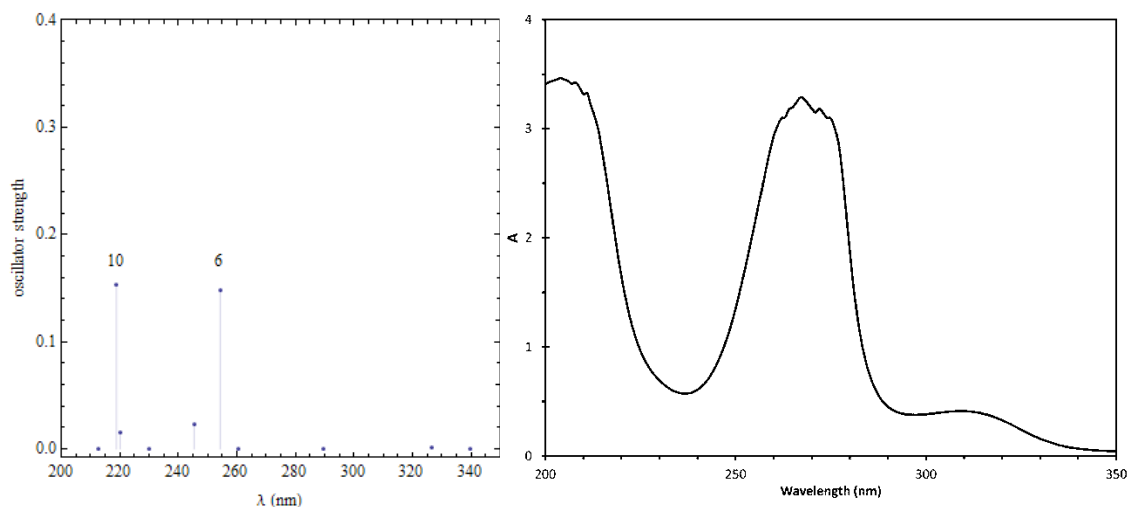


Figure 25. Calculated and experimental (curve) UV spectra of Hpzc in water.

The 254 nm line in the simulated spectra corresponds to an electronic transition to state 6, and the line at 219 nm corresponds to a transition to state 10. There are two dominant NTO hole/particle pairs for each of these transitions, shown in **Figure 26**. The first NTO pair represents 12% of the transition and the second pair has a weight of 88%, while the two NTO pairs corresponding to the higher energy transition have weights of 10% and 88%. In both transitions, the hole for the dominant NTO pair shows a strong π bonding character. Additionally, there is also a non-negligible π bonding contribution from the carbonyl group. The corresponding NTO particles are clearly π^* anti-bonding, and these transitions are classified as $\pi \rightarrow \pi^*$ type transitions.

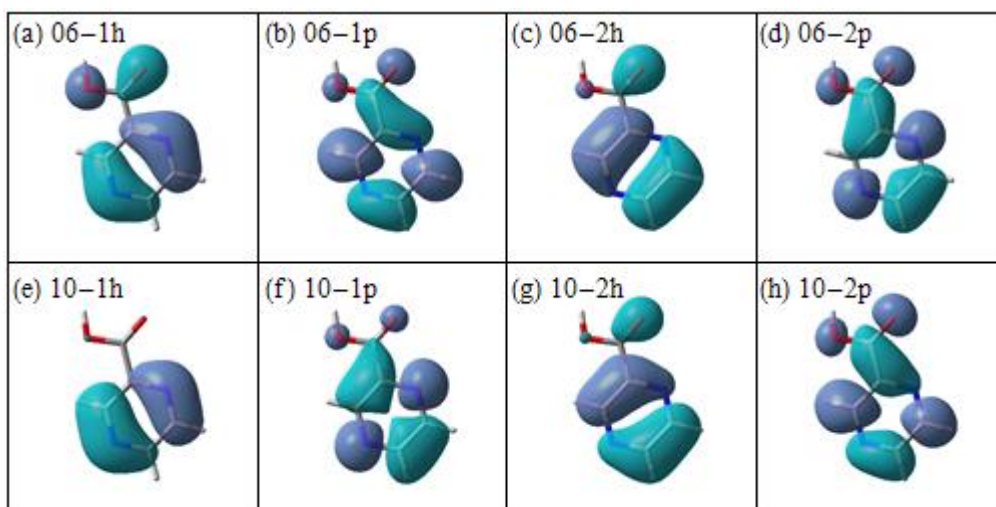


Figure 26. NTO hole/particle pairs for the electronic transitions of Hpzc at 254 and 219 nm.

btc and pzc ions in water

The simulated electronic spectra for both the btc ion, and pzc ion in water are shown in **Figure 27**. The calculated spectrum of the pzc ion in water is not significantly different from hpzc in water, and similarly the observed experimental band at 312 nm could not be identified from this calculation. However, in the case of the btc ion the 323 nm line at low energy could possibly correspond to the very weak observed band in the experimental spectrum at 294 nm. Although the calculated transition is significantly lower in energy, this seems to be the only transition for H₃btc or btc with a significant oscillator strength and a wavelength greater than 280 nm.

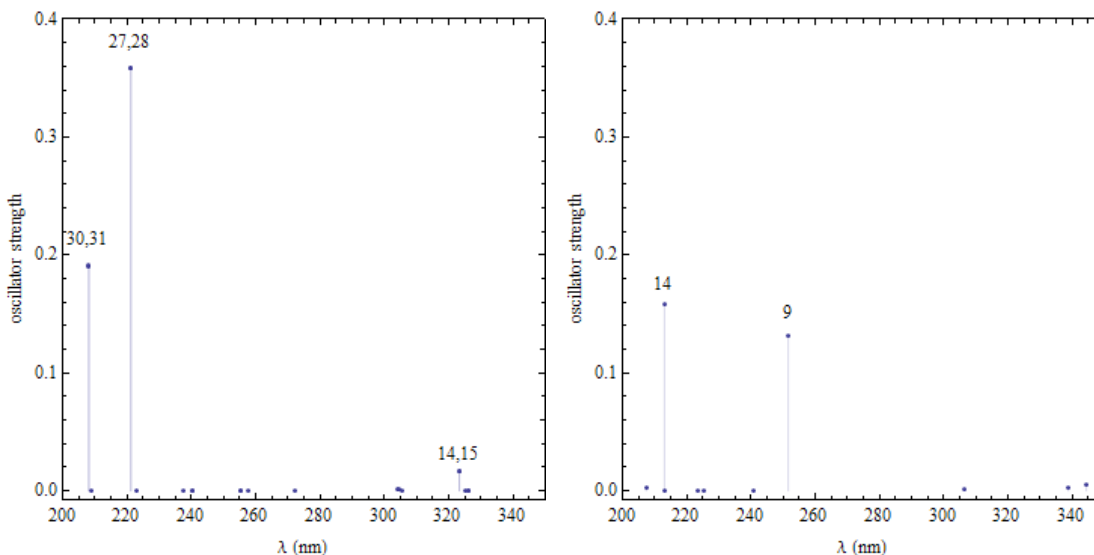


Figure 27. Calculated UV spectrum of btc ion (left) and pzc ion (right) in water.

The calculated 323 nm line of the btc anion is due to transitions to states 14 and 15. The NTO hole/particle pairs for these transitions are shown in **Figure 28**. There are two dominant NTO pairs for each transition. The weights for state 14 are 24% and 76%, for NTO pairs 1 and 2 respectively, and the weights for state 15 are 21% and 79% for NTO pairs 1 and 2, respectively. The NTO holes appear to resemble p-type lone pair orbitals on the oxygen atoms. However, closer inspection shows that for each hole the phase on adjacent oxygen atoms are opposite of one another. This is likely to due to the anti-symmetric combination of two neighboring carbon-oxygen π -type bonds, such that there is a node on the bridging carbon atom. The corresponding particles have a π^* anti-bonding pattern within the phenyl ring. These transitions are thus identified as $\pi \rightarrow \pi^*$ type.

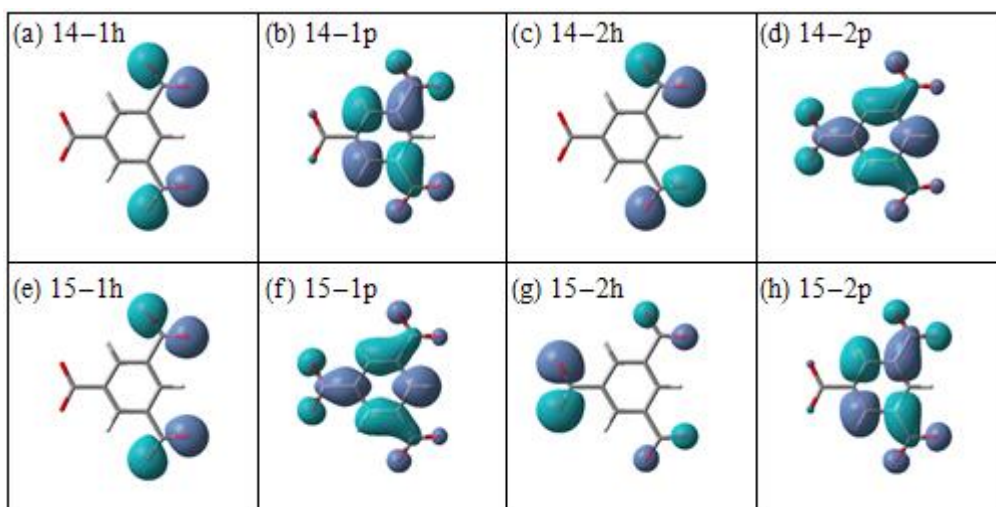


Figure 28. NTO hole/particle pairs for the electronic transitions of btc ion at 323 nm.

The remaining high energy spectral lines at 221 nm and 208 nm are identified similarly to their corresponding calculated H₃btc transitions. However, additional nodes are produced, again likely due to molecular symmetry.

The line at 221 nm is due to transitions to excited states 27 and 28. The two NTO hole/particle pairs for both of these transitions are shown in **Figure 29**. The weights are 45%-45% for pairs 1 and 2, respectively, for both states 27 and 28. The NTO holes have a π bonding character and the NTO particles are π^* , and as mentioned are identified as $\pi \rightarrow \pi^*$ type transitions.

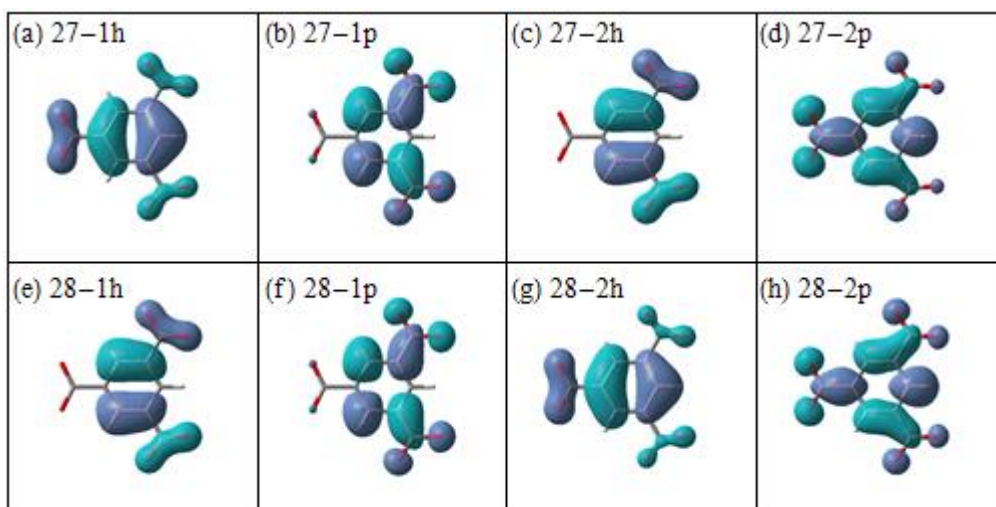


Figure 29. NTO hole/particle pairs for the electronic transitions of btc ion at 221 nm.

The highest energy line at 208 nm is due to transitions to excited states 30 and 31, and there is only one NTO hole/particle pair with a weight of 83% for each state. The NTO pairs are shown in **Figure 30**. The NTO holes for both states are similar to the anti-symmetric combination of carbon-oxygen π bonds observed on the carbonyl groups, and the corresponding particles are high energy π^* anti-bonding orbitals with several nodes. This line is classified as a $\pi \rightarrow \pi^*$ transition.

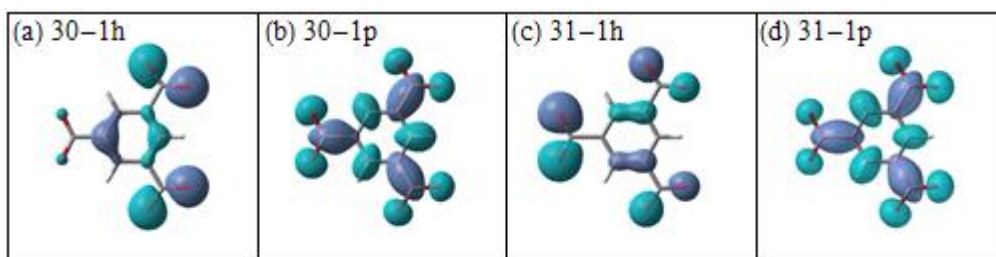


Figure 30. NTO hole/particle pairs for the electronic transitions of btc ion at 208 nm.

Compound 1

A series of TD-DFT calculations were also performed on btc and pzc using molecular geometries taken directly from the SXRD crystal structure for compound **1**. These calculations were performed for both the anions and, with the anions in an

electrostatic potential field of calcium ions represented as static (2+) charges. The simulated spectra for these calculations are compared in **Figure 31**. Panels (a) and (b) show the spectra for the bare btc ion in compound **1**, and the bare pzc ion in compound **1**, respectively. Panels (c) and (d) show the calculated spectra including calcium ions as charges. Indeed, the electronic transitions are modified by the presence of the charges; however, the resulting spectra do not seem to correlate with the observed UV VIS spectra for these compounds. Although, the btc ion from compound **1** shows a number of states between 240 and 350 nm that may be connected with observed absorption bands; the calculated oscillator strengths are not in good agreement with the experimental data.

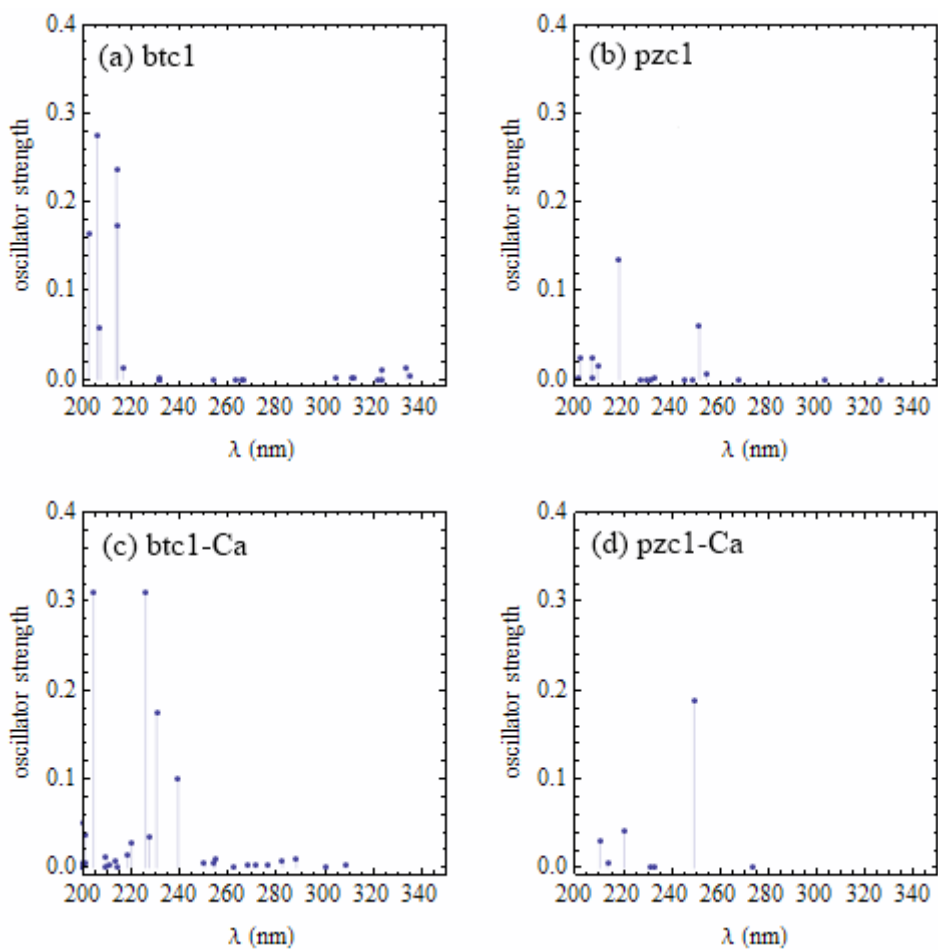


Figure 31. Calculated UV spectra for btc and pzc molecular structures extracted from SXR data. Panels (a)-(b) do not include calcium ion charges and panels (c)-(d) do include calcium ion charges.

Coordination Environments

Additionally, TD-DFT calculations were performed on non-optimized SXRD derived asymmetric units, as shown in **Figure 19.**, without vicinal waters. The fully local M06L functional,⁴² and the hybrid PBE/PBE functional were used both with and without the long-range correction (lc-) of Iikura *et. al.*,⁶⁴ and with both the LANL2DZ⁶⁵ and the cc-pVDZ basis sets. Convergence errors were observed for the asymmetric unit when utilizing the lc-M06L/cc-pVDZ, lc-M06L/LANL2DZ, M06L/cc-pVDZ, and lc-pbepbe/cc-pVDZ model chemistries. For these structures, molecular orbital coefficient and valence-core electron mixing errors were encountered.

Due to the orientation of the aromatic rings in the asymmetric unit, planar isomers as well as extended coordination environments (without overlapping aromatic rings) were also attempted. Calculations completed normally for geometries comprised of asymmetric units which were planar, and for a planar asymmetric unit with a full calcium environment as shown in **Figure 32.** For this structure, calculations terminated normally using the lc-M06L/LANL2DZ and M06L/cc-pVDZ model chemistries. However, the first several states produced by both methods were unusually low in energy, corresponding to some visible and several IR transitions, which are not experimentally reasonable. NTO hole-particle pairs of these states were Rydberg in nature,⁶⁶ and in coordination environments with all of the calcium atoms included, electron density was observed between calcium atoms where the carboxylate groups of overlapping aromatic rings would typically bridge, shown in **Figure 32.**

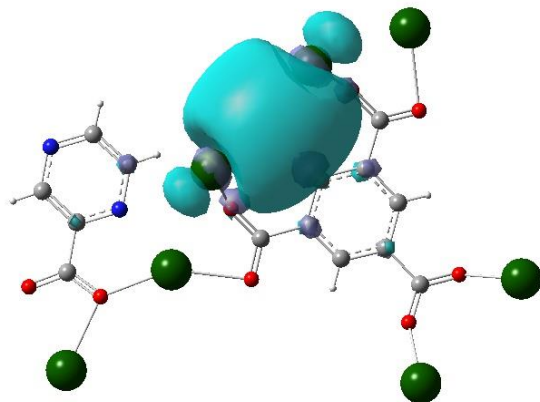


Figure 32. Rydberg particle state at 850 nm of a planar asymmetric unit of (1) with full Calcium coordination environment.

Considering the periodic environment of the experimental structure, these states could not be entirely discarded as artifacts nor determined to be independent of the other states. A more detailed model of the coordination environment, which explicitly includes water molecules, vicinal Ca^{2+} atoms (or representative charges), or one that is able to accommodate overlapping aromatic ligands, may be necessary to reproduce the experimental spectrum.

Benchmark Calculations with Pseudopotential Basis Sets

The MOF coordination environments whose TD-DFT calculations terminated normally with Rydberg hole-particle states, suggested that other pseudopotential basis sets could be investigated as methods to predict electronic structure in hybrid compounds. A computational approach that could predict the electronic structure of small heavy-metal-organic compounds, should be used to as a starting point to investigate larger systems. Based on the need for a further developed approach to accommodate heavier atoms into organic systems, a general method was developed to predict the UV-Vis spectra of organic-lanthanide complexes with TD-DFT.

Using approaches for polyoxometalates and hybrid transition-metal systems, several basis sets, functionals, and levels of theory were attempted on small lanthanide heterometallic oxides and organic lanthanides containing the smaller atoms, cerium, dysprosium and neodymium. The purpose of this was to determine if known approaches could be adjusted to theoretical targets. Although calculations completed for arbitrary geometries of one lanthanide in simple coordination environments with oxygen and hydrogen, applying methods intended for larger systems such as mixing the basis sets LANL2DZ, Def-2TZVP, WTBS, SARC-ZORA, and CRENL, hybrid functionals such as BP86, PBEPBE, X3LYP, M06L, and long-range corrections, extended geometries were generally unsuccessful.^{41, 67-73} Common errors similarly included convergence failures, core-valence electron mixing, and difficulties with the DFT grids.

Based on the optimization and transition state work of Okuda et. al., and Qu et. al.^{74,75} the Stuttgart-Dresden pseudopotential (SDD) basis sets³⁸⁻⁴⁰ included in Gaussian09 were applied as benchmark test and excited state calculations were carried⁷⁶ out for a small, well-known organic-lanthanide complex, europium acetate. The X3LYP functional was used, and when SDD basis sets were applied to the entire molecule, transitions were observed which corresponded to the larger intensity transitions of europium acetate, shown in **Figure 33**.

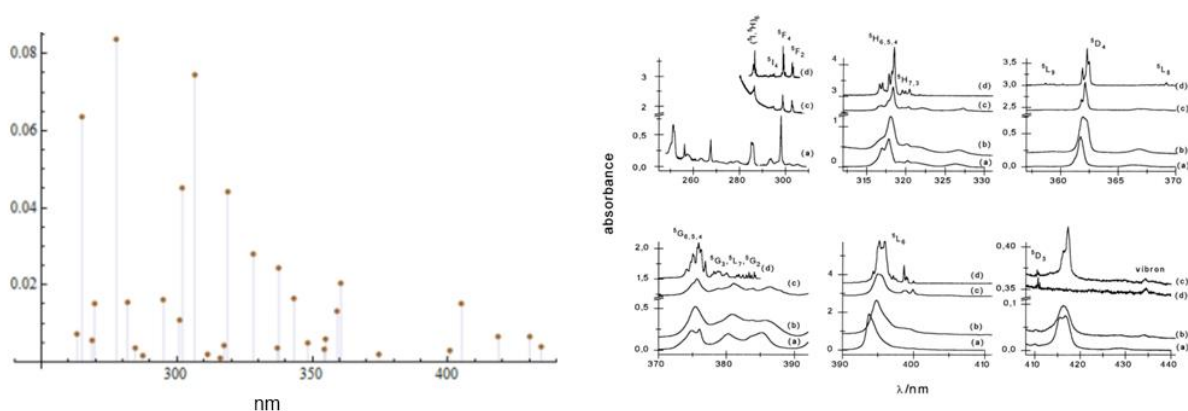


Figure 33. Calculated and experimental(left) UV spectra of Eu^{III} -aquoion (a), Eu^{III} -acetate complex in solution (b) and in the crystal at 293 K (c) and at 4K (d).

Different coordination numbers are possible for one lanthanide atom, and choosing an appropriate coordination number, i.e. how many additional oxygen atoms are bonded to the lanthanide, affects spectral detail. Notably, more peaks are observed as additional, smaller intensity transitions, when the coordination number was nine, versus seven for optimized $\text{Eu}(\text{COOH})_3$ geometries.

$\text{Eu}(\text{NO}_3)_3$, which forms complexes in aqueous solution, was also used to benchmark the pseudopotential basis set method, and explore the compatibility of a solvation model. The electronic and experimental spectra of $\text{Eu}(\text{NO}_3)_3$ are in good agreement, and are shown in **Figure 34**.

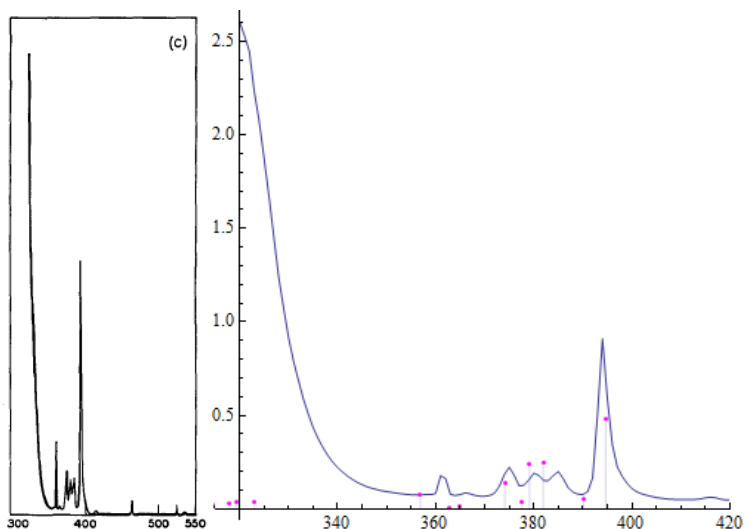


Figure 34. Experimental standard(left) and experimental (curve) vs. TD-DFT(magenta) (right) spectra UV spectra of $\text{Eu}(\text{NO}_3)_3$ in water.

To test this method for use in a lanthanide POM system, a theoretical lanthanide hexaniobate cluster, $\text{Eu-Nb}_6\text{O}_{19}$, was constructed using the crystal structure of Nb_6O_{19} . The structure successfully optimized, and TD-DFT was carried out on the optimized geometry. NTO analysis was applied to the TD-DFT results of the $\text{Eu-Nb}_6\text{O}_{19}$ cluster to qualitatively represent regions of electron density transfer (**Figure 35**).

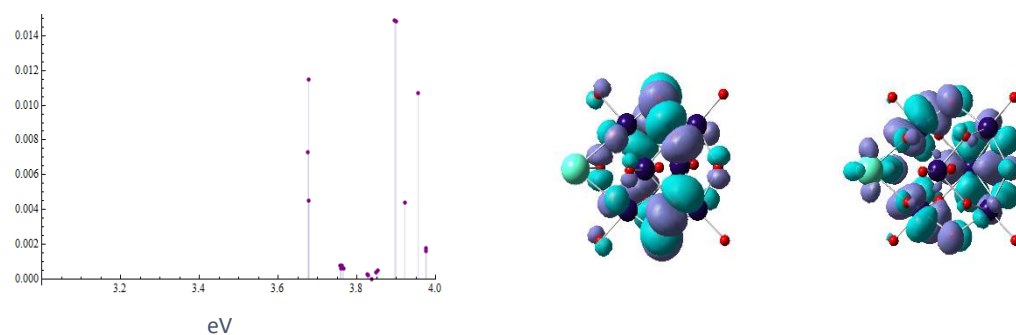


Figure 35. (left) TD-DFT spectra of theoretical $\text{Eu-Nb}_6\text{O}_{19}$ cluster (y axis = f) using SDD basis sets. NTO pair (center & right) of the first excited state at $3.677\text{eV}/337.19\text{ nm}$. The ground state “hole” (center) and the excited state “particle” (right) of $\text{Eu-Nb}_6\text{O}_{19}$ show regions of electron density transfer composing 100% of the calculated transition.

These results represent the first successful TD-DFT calculation, and NTO analysis of a lanthanide POM. This method could be used to explain electron transfer in emerging POMs, and thus be used to pre-design new systems with electronic properties optimized for green energy applications.

REFERENCES

1. Blankenship, R. E.; Tiede, D. M.; Barber, J.; Brudvig, G. W.; Fleming, G.; Ghirardi, M.; Gunner, M. R.; Junge, W.; Kramer, D. M.; Melis, A.; Moore, T. A.; Moser, C. C.; Nocera, D. G.; Nozik, A. J.; Ort, D. R.; Parson, W. W.; Prince, R. C.; Sayre, R. T., Comparing Photosynthetic and Photovoltaic Efficiencies and Recognizing the Potential for Improvement. *Science* **2011**, 332 (6031), 805-809.
2. Analysis of the Clean Energy Standard Act of 2012, U.S. Department of Energy, **2012**, May.
3. Bogani, L.; Wernsdorfer, W. Molecular spintronics using single-molecule magnets. *Nature Materials*. **2008**, 7, 179-186.
4. Binnemans, K. Lanthanide-based luminescent hybrid materials. *Chemical Reviews*. **2009**, 109, 4283-4374.
5. Nyman, M. Polyoxoniobate chemistry in the 21st century. *Dalton Transactions*. **2011**, 40, 8049-8058.
6. Ma, Y.; Xu, G. F.; Yang, X.; Li, L. C.; Tang, J.; Yan, S. P.; Cheng, P.; Liao, D. Z. Pyrazine-bridged Dy²⁺ single-molecule magnet with a large anisotropic barrier. *Chemical Communications*.. **2010**, 46, 8264-8266.
7. Martin, R. L. Natural transition orbitals. *Journal of Chemical Physics*. **2003**, 118, 4775-4777.
8. Dinca, M.; Dailly, A.; Liu, Y.; Brown, C. M.; Neumann, D. A.; Long, J. R. Hydrogen storage in a microporous metal-organic framework with exposed Mn²⁺ coordination sites. *Journal of the American Chemical Society*. **2006**, 128, 16876-16883.
9. Lu, H.-F.; Yan, B.; Liu, J.-L. Functionalization of Calix[4]arene as a Molecular Bridge To Assemble Luminescent Chemically Bonded Rare-Earth Hybrid Systems. *Inorganic Chemistry*. **2009**, 48, 3966-3975.
10. Cahill, C. L.; de Lill, D. T.; Frisch, M. Homo- and heterometallic coordination polymers from the f elements. *CrystEngComm*. **2007**, 9, 15-26.
11. Tian, C.-h.; Sun, Z.-g.; Li, J.; Zheng, X.-f.; Liang, H.-d.; Zhang, L.-c.; You, W.-s.; Zhu, Z.-m. Synthesis and crystal structures of two new inorganic-organic hybrid polyoxomolybdate complexes: [Himi]₄[{Co(imi)₂(H₂O)₂}Mo₇O₂₄·4H₂O and [Zn(imi)₄]₂[(imi)₂Mo₈O₂₆·6H₂O. *Inorganic Chemistry Communications*. **2007**, 10, 757-761.
12. Chen, Q.; Cai, C.; Zhou, G.; Xu, Y.; Zhu, D.; Zheng, X. Hydrothermal Synthesis and Structure of a New Three-Dimensional Inorganic-Organic Hybrid Polyoxomolybdate

Based on Keggin Cluster Units. *Zeitschrift Fur Anorganische Und Allgemeine Chemie*. **2008**, 634, 1197-1200.

13. Fan, L.-M.; Li, D.-C.; Wei, P.-H.; Liu, G.-Z.; Zhang, X.-T.; Dou, J.-M. Exploratory syntheses and structural characterizations of three organic-inorganic hybrid polyoxomolybdate frameworks linked by M(II)-Ln units (M = Ni, Co, Zn; L = 2,2'-biimidazole). *Journal of Coordination Chemistry*. **2011**, 64, 2531-2544.

14. An, H.; Xiao, D.; Wang, E.; Li, Y.; Xu, L. A series of new polyoxoanion-based inorganic-organic hybrids: $(C_6NO_2H_5)[(H_2O)_4(C_6NO_2H_5)Ln(CrMo_6H_6O_{24})] \cdot 4H_2O$ (Ln = Ce, Pr, La and Nd) with a chiral layer structure. *New Journal of Chemistry*. **2005**, 29, 667-672.

15. An, H.; Li, Y.; Xiao, D.; Wang, E.; Sun, C. Self-Assembly of Extended High-Dimensional Architectures from Anderson-type Polyoxometalate Clusters. *Crystal Growth & Design*. **2006**, 6, 1107-1112.

16. Naruke, H.; Yamase, T. Structural investigation of $R_2Mo_4O_{15}$ (R=La, Nd, Sm), and polymorphs of the $R_2Mo_4O_{15}$ (R=rare earth) family. *Journal of Solid State Chemistry*. **2003**, 173, 407-417.

17. Burgemeister, K.; Drewes, D.; Limanski, Eva M.; Küper, I.; Krebs, B. Formation of Large Clusters in the Reaction of Lanthanide Cations with Heptamolybdate. *European Journal of Inorganic Chemistry*. **2004**, 2004, 2690-2694.

18. Wang, H.-Y.; Zhang, C.-J.; Zhang, C.-H.; Tang, Q.; Chen, Y.-G. Synthesis, structure, and magnetism of four polyoxomolybdate compounds containing yttrium and ytterbium. *Journal of Coordination Chemistry*. **2011**, 64, 1481-1490.

19. Zhang, Z.; Xu, Y.; Zheng, L.; Zhu, D.; Song, Y. $\{[V^{IV}_{14}V^V_4O_{42}(H_2O)][Ni(C_4N_3H_{13})(C_4N_3H_{14})]_4(H_2O)_6\}^{4+}$: a novel nanosized calix-type polyoxovanadate cation. *CrystEngComm*. **2011**, 13, 2191-2193.

20. Liu, J. L.; Zhou, Y. Z. Synthesis, Structures and Properties of Inorganic-Organic Polyoxovanadate. *Progress in Chemistry*. **2010**, 22, 51.

21. Guo, Y. N.; Xu, G. F.; Wernsdorfer, W.; Ungur, L.; Guo, Y.; Tang, J.; Zhang, H. J.; Chibotaru, L. F.; Powell, A. K. Strong axiality and Ising exchange interaction suppress zero-field tunneling of magnetization of an asymmetric Dy_2 single-molecule magnet. *Journal of the American Chemical Society*. **2011**, 133, 11948-11951.

22. Hayashi, Y. Hetero and lacunary polyoxovanadate chemistry: Synthesis, reactivity and structural aspects. *Coordination Chemistry Reviews*. **2011**, 255, 2270-2280.

23. Yan, B.; Wang, Q.-M.; Ma, D.-J. Molecular Construction, Characterization, and Photophysical Properties of Supramolecular Lanthanide–Calix[4]arene Covalently Bonded Hybrid Systems. *Inorganic Chemistry*. **2008**, *48*, 36-44.
24. Nyman, M.; Criscenti, L. J.; Bonhomme, F.; Rodriguez, M. A.; Cygan, R. T. Synthesis, structure, and molecular modeling of a titanoniobate isopolyanion. *Journal of Solid State Chemistry*. **2003**, *176*, 111-119.
25. Anderson, T. M.; Thoma, S. G.; Bonhomme, F.; Rodriguez, M. A.; Park, H.; Parise, J. B.; Alam, T. M.; Larentzos, J. P.; Nyman, M. Lithium Polyniobates. A Lindqvist-Supported Lithium–Water Adamantane Cluster and Conversion of Hexaniobate to a Discrete Keggin Complex. *Crystal Growth & Design*. **2007**, *7*, 719-723.
26. Yamase, T.; Kobayashi, T.; Kettle, S. F. A. Inframolecular Energy Transfer and Mn⁴⁺ Luminescence in Polyoxometallomanganate Lattices. *Journal of The Electrochemical Society*. **1996**, *143*, 1678-1680.
27. Yamase, T. *Polyoxometalate Chemistry From Topology via Self-Assembly to Applications*; Pope, M., Müller, A., Eds.; Springer Netherlands: 2002, p 187.
28. Antonio, M. R.; Nyman, M.; Anderson, T. M. Direct Observation of Contact Ion-Pair Formation in Aqueous Solution. *Angewandte Chemie International Edition*. **2009**, *48*, 6136-6140.
29. Nyman, M.; Bonhomme, F.; Alam, T. M.; Rodriguez, M. A.; Cherry, B. R.; Krumhansl, J. L.; Nenoff, T. M.; Sattler, A. M. A General Synthetic Procedure for Heteropolyniobates. *Science*. **2002**, *297*, 996-998.
30. Ohlin, C. A.; Villa, E. M.; Casey, W. H. One-pot synthesis of the decaniobate salt [N(CH₃)₄]₆[Nb₁₀O₂₈]·6H₂O from hydrous niobium oxide. *Inorganica Chimica Acta*. **2009**, *362*, 1391-1392.
31. Chen, G.; Ma, P.; Wang, J.; Niu, J. A new organic–inorganic hybrid polyoxoniobate based on Lindqvist-type anion and nickel complex. *Journal of Coordination Chemistry*. **2010**, *63*, 3753-3763.
32. Niu, J.; Wang, G.; Zhao, J.; Sui, Y.; Ma, P.; Wang, J. Zero- or One-Dimensional Organic–Inorganic Hybrid Polyoxoniobates Constructed from Decaniobate Units and Transition-Metal Complexes. *Crystal Growth & Design*. **2011**, *11*, 1253-1261.
33. Son, J. H.; Ohlin, C. A.; Casey, W. H. A new class of soluble and stable transition-metal-substituted polyoxoniobate: [Cr₂(OH)₄Nb₁₀O₃₀]⁸⁻. *Dalton Transactions*. **2012**, *41*, 12674-12677.
34. Vila-Nadal, L.; Wilson, E. F.; Miras, H. N.; Rodriguez-Forteza, A.; Cronin, L.; Poblet, J. M. Combined theoretical and mass spectrometry study of the formation-fragmentation of small polyoxomolybdates. *Inorg Chem*. **2011**, *50*, 7811-7819.

35. Ravelli, D.; Dondi, D.; Fagnoni, M.; Albini, A.; Bagno, A. Predicting the UV spectrum of polyoxometalates by TD-DFT. *J Comput Chem.* **2011**, *32*, 2983-2987.
36. Gaussian 09, Revision A.1, Frisch, M. J.; Trucks, G. W.; Schlegel, H. B.; Scuseria, G. E.; Robb, M. A.; Cheeseman, J. R.; Scalmani, G.; Barone, V.; Mennucci, B.; Petersson, G. A.; Nakatsuji, H.; Caricato, M.; Li, X.; Hratchian, H. P.; Izmaylov, A. F.; Bloino, J.; Zheng, G.; Sonnenberg, J. L.; Hada, M.; Ehara, M.; Toyota, K.; Fukuda, R.; Hasegawa, J.; Ishida, M.; Nakajima, T.; Honda, Y.; Kitao, O.; Nakai, H.; Vreven, T.; Montgomery, Jr., J. A.; Peralta, J. E.; Ogliaro, F.; Bearpark, M.; Heyd, J. J.; Brothers, E.; Kudin, K. N.; Staroverov, V. N.; Kobayashi, R.; Normand, J.; Raghavachari, K.; Rendell, A.; Burant, J. C.; Iyengar, S. S.; Tomasi, J.; Cossi, M.; Rega, N.; Millam, J. M.; Klene, M.; Knox, J. E.; Cross, J. B.; Bakken, V.; Adamo, C.; Jaramillo, J.; Gomperts, R.; Stratmann, R. E.; Yazyev, O.; Austin, A. J.; Cammi, R.; Pomelli, C.; Ochterski, J. W.; Martin, R. L.; Morokuma, K.; Zakrzewski, V. G.; Voth, G. A.; Salvador, P.; Dannenberg, J. J.; Dapprich, S.; Daniels, A. D.; Farkas, Ö.; Foresman, J. B.; Ortiz, J. V.; Cioslowski, J.; Fox, D. J. Gaussian, Inc., Wallingford CT, 2009.
37. Perdew, J. P.; Burke, K.; Ernzerhof, M., Generalized gradient approximation made simple. *Physical Review Letters* **1996**, *77* (18), 3865-3868.
38. Leininger, T.; Berning, A.; Nicklass, A.; Stoll, H.; Werner, H. J.; Flad, H. J. Spin-orbit interaction in heavy group 13 atoms and TI Ar. *Chemical Physics.* **1997**, *217*, 19-
39. Dolg, M.; Wedig, U.; Stoll, H., Preuss; H.J., Modern Methods and Algorithms of Quantum Chemistry, *Chemical Physics* **2000**, *86*, 8661987.
40. Kuchle, W.; Dolg, M.; Stoll, H.; Preuss, H., Pseudopotentials of the Stuttgart/Dresden Group. See: www.theochem.uni-stuttgart.de/pseudopotentiale.
41. Perdew, J. P., Density- functional approximation for the correlation- energy of the inhomogeneous electron-gas. *Physical Review B.* **1986**, *33* (12), 8822-8824.
42. Zhao, Y.; Truhlar, D. G., A new local density functional for main-group thermochemistry, transition metal bonding, thermochemical kinetics, and noncovalent interactions. *Journal of Chemical Physics* **2006**, *125* (19).
43. Fromm, K. M., Coordination polymer networks with s-block metal ions. *Coordination Chemistry Reviews* **2008**, *252* (8-9), 856-885.
44. Lan, J. H.; Cao, D. P.; Wang, W. C.; Smit, B., Doping of Alkali, Alkaline-Earth, and Transition Metals in Covalent-Organic Frameworks for Enhancing CO₂ Capture by First-Principles Calculations and Molecular Simulations. *Acs Nano* **2010**, *4* (7), 4225-4237.

45. Han, S. S.; Goddard, W. A., Lithium-Doped Metal-Organic Frameworks for Reversible H₂ Storage at Ambient Temperature. *Journal of the American Chemical Society* **2007**, *129* (27), 8422-8423.
46. Pan, L.; Frydel, T.; Sander, M. B.; Huang, X. Y.; Li, J., The effect of pH on the dimensionality of coordination polymers. *Inorganic chemistry* **2001**, *40* (6), 1271-1283.
47. Yang, Y. Y.; Huang, Z. Q.; Szeto, L.; Wong, W. T., A two-dimensional layer structure containing calcium: Ca-3(1,3,5-benzenetricarboxylate)(2)(H₂O)(12)(n). *Applied Organometallic Chemistry* **2004**, *18* (2), 97-98.
48. Nielsen, R. K. B.; Kongshaug, K. O.; Fjellvag, H., Syntheses, crystal structures and thermal properties of 3D coordination polymers assembled from 1,4,5,8-naphthalenetetracarboxylic acid. *Solid State Sciences* **2006**, *8* (10), 1237-1242.
49. Fei, Z. F.; Geldbach, T. J.; Scopelliti, R.; Dyson, P. J., Metal-organic frameworks derived from imidazolium dicarboxylates and group I and II salts. *Inorganic chemistry* **2006**, *45* (16), 6331-6337.
50. Volkringer, C.; Loiseau, T.; Ferey, G.; Warren, J. E.; Wragg, D. S.; Morris, R. E., A new calcium trimellitate coordination polymer with a chain-like structure. *Solid State Sciences* **2007**, *9* (6), 455-458.
51. Shuai, Q.; Chen, S.; Gao, S., Structural and thermal properties of three novel alkaline earth metal coordination polymers based on 5-hydroxyisophthalate ligand. *Inorganica Chimica Acta* **2007**, *360* (5), 1381-1387.
51. Williams, C. A.; Blake, A. J.; Wilson, C.; Hubberstey, P.; Schroeder, M., Novel metal-organic frameworks derived from group II metal cations and aryldicarboxylate anionic ligands. *Crystal Growth & Design* **2008**, *8* (3), 911-922.
52. Volkringer, C.; Marrot, J.; Ferey, G.; Loiseau, T., Hydrothermal crystallization of three calcium-based hybrid solids with 2,6-naphthalene- or 4,4'-biphenyl-dicarboxylates. *Crystal Growth & Design* **2008**, *8* (2), 685-689.
53. Liu, W. S.; Jiao, T. Q.; Li, Y. Z.; Liu, Q. Z.; Tan, M. Y.; Wang, H.; Wang, L. F., Lanthanide coordination polymers and their Ag⁺-modulated fluorescence. *Journal of the American Chemical Society* **2004**, *126* (8), 2280-2281.
54. Vakiti, R. K.; Garabato, B. D.; Schieber, N. P.; Rucks, M. J.; Cao, Y.; Webb, C.; Maddox, J. B.; Celestian, A.; Pan, W.-P.; Yan, B. Synthesis and Characterization of Two- and Three-Dimensional Calcium Coordination Polymers Built with Benzene-1,3,5-tricarboxylate and/or Pyrazine-2-carboxylate. *Crystal Growth & Design*. **2012**, *12*, 3937-3943.
55. Tomasi, J.; Mennucci, B.; Cammi, R., Quantum mechanical continuum solvation models. *Chemical reviews* **2005**, *105* (8), 2999-3093.

56. Dunning, T. H., Gaussian-basis sets for use in correlated molecular calculations of the atoms boron through neon and hydrogen. *Journal of Chemical Physics* **1989**, *90* (2), 1007-1023.
57. Bauernschmitt, R.; Ahlrichs, R., Treatment of electronic excitations within the adiabatic approximation of time dependent density functional theory. *Chemical Physics Letters* **1996**, *256* (4-5), 454-464.
58. Casida, M. E.; Jamorski, C.; Casida, K. C.; Salahub, D. R., Molecular excitation energies to high-lying bound states from time-dependent density-functional response theory: Characterization and correction of the time-dependent local density approximation ionization threshold. *Journal of Chemical Physics* **1998**, *108* (11), 4439-4449.
59. Stratmann, R. E.; Scuseria, G. E.; Frisch, M. J., An efficient implementation of time-dependent density-functional theory for the calculation of excitation energies of large molecules. *Journal of Chemical Physics* **1998**, *109* (19), 8218-8224.
60. Van Caillie, C.; Amos, R. D., Geometric derivatives of excitation energies using SCF and DFT. *Chemical Physics Letters* **1999**, *308* (3-4), 249-255.
61. Van Caillie, C.; Amos, R. D., Geometric derivatives of density functional theory excitation energies using gradient-corrected functionals. *Chemical Physics Letters* **2000**, *317* (1-2), 159-164.
62. Furche, F.; Ahlrichs, R., Adiabatic time-dependent density functional methods for excited state properties. *Journal of Chemical Physics* **2002**, *117* (16), 7433-7447.
63. Scalmani, G.; Frisch, M. J.; Mennucci, B.; Tomasi, J.; Cammi, R.; Barone, V., Geometries and properties of excited states in the gas phase and in solution: Theory and application of a time-dependent density functional theory polarizable continuum model. *Journal of Chemical Physics* **2006**, *124* (9).
64. Iikura, H.; Tsuneda, T.; Yanai, T.; Hirao, K., A long-range correction scheme for generalized-gradient-approximation exchange functionals. *Journal of Chemical Physics* **2001**, *115* (8), 3540-3544.
65. Wadt, W. R.; Hay, P. J., Abinitio effective core potentials for molecular calculations - potentials for main group elements Na to Bi. *Journal of Chemical Physics* **1985**, *82* (1), 284-298.
66. Dreuw, A.; Head-Gordon, M., Single-reference ab initio methods for the calculation of excited states of large molecules. *Chemical reviews* **2005**, *105* (11), 4009-4037. (b)

67. Weigend, F.; Ahlrichs, R., Balanced basis sets of split valence, triple zeta valence and quadruple zeta valence quality for H to Rn: Design and assessment of accuracy. *Physical Chemistry Chemical Physics* **2005**, 7 (18), 3297-3305.
68. Huzinaga, S.; Klobukowski, M., Well-tempered Gaussian basis sets for the calculation of matrix Hartree-Fock wavefunctions. *Chemical Physics Letters* **1993**, 212 (3-4), 260-264.
69. Pantazis, D. A.; Neese, F., All-Electron Scalar Relativistic Basis Sets for the Lanthanides. *Journal of Chemical Theory and Computation* **2009**, 5 (9), 2229-2238.
70. Lajohn, L. A.; Christiansen, P. A.; Ross, R. B.; Atashroo, T.; Ermler, W. C., Abinitio relativistic effective potentials with spin orbit operators .3. Rb through Xe. *Journal of Chemical Physics* **1987**, 87 (5), 2812-2824.
71. Becke, A. D., Density-functional exchange-energy approximation with correct asymptotic behavior. *Physical Review A* **1988**, 38 (6), 3098-3100.
72. Perdew, J. P.; Burke, K.; Ernzerhof, M., Generalized gradient approximation made simple. *Physical Review Letters* **1996**, 77 (18), 3865-3868.
73. Xu, X.; Goddard, W. A., The X3LYP extended density functional for accurate descriptions of nonbond interactions, spin states, and thermochemical properties. *Proceedings of the National Academy of Sciences of the United States of America* **2004**, 101 (9), 2673-2677.
74. Venugopal, A.; Fegler, W.; Spaniol, T. P.; Maron, L.; Okuda, J., Dihydrogen Addition in a Dinuclear Rare-Earth Metal Hydride Complex Supported by a Metalated TREN Ligand. *Journal of the American Chemical Society* **2011**, 133 (44), 17574-17577.
75. Kang, X. H.; Song, Y. M.; Luo, Y.; Li, G.; Hou, Z. M.; Qu, J. P., Computational Studies on Isospecific Polymerization of 1-Hexene Catalyzed by Cationic Rare Earth Metal Alkyl Complex Bearing a C-3 iPr-trisox Ligand. *Macromolecules* **2012**, 45 (2), 640-651.
76. Bukietynska, K.; Mondry, A., f-f Transition intensities of europium(III) acetate complexes in a single crystal and in solution. *Journal of Alloys and Compounds* **2001**, 323, 150-154.
77. Hohenberg, P.; Kohn, W., Inhomogeneous Electron Gas. *Physical Review B* **1964**, 136, 864. (b) Kohn, W.; Sham, L.J., Self-Consistent Equations Including Exchange and Correlation Effects. *Physical Review A* **1965**, 1133.
78. Jensen, F. *Introduction to Computational Chemistry* **1999** Wiley, New York.

79.Szabo A.; Otslund N., *Modern Quantum Chemistry: Introduction to Advanced Electronic Structure Theory* **1996**, Dover.

80.Marques, M.A.L.; Ullrich, C.A.; Nogueira, F.; Rubio, A.; Burke, K.; Gross, E. K.U., *Time-Dependent Density Functional Theory* **2006**, Springer.

